Groove-induced changes of discharge in channel flows

Yu Chen[1,2,†], J. M. Floryan[3], Y. T. Chew[1] and B. C. Khoo[1]

[1]Department of Mechanical Engineering, National University of Singapore, 9 Engineering Drive 1,
Singapore 117575, Singapore

[2]Institute of High Performance Computing, Agency for Science, Technology and Research,
1 Fusionopolis Way, #16-16 Connexis, Singapore 138632, Singapore

[3]Department of Mechanical and Materials Engineering, The University of Western Ontario, London,
Ontario, N6A5B9, Canada

The changes in discharge in pressure-driven flows through channels with longitudinal grooves have been investigated in the laminar flow regime and in the turbulent flow regime with moderate Reynolds numbers ($Re_{2H} \approx 6000$) using both analytical and numerical methodologies. The results demonstrate that the long-wavelength grooves can increase discharge by 20 %–150 %, depending on the groove amplitude and the type of flow, while the short-wavelength grooves reduce the discharge. It has been shown that the reduced geometry model applies to the analysis of turbulent flows and the performance of grooves of arbitrary form is well approximated by the performance of grooves whose shape is represented by the dominant Fourier mode. The flow patterns, the turbulent kinetic energy as well as the Reynolds stresses were examined to identify the mechanisms leading to an increase in discharge. It is shown that the increase in discharge results from the rearrangement of the bulk fluid movement and not from the suppression of turbulence intensity. The turbulent kinetic energy and the Reynolds stresses are rearranged while their volume-averaged intensities remain the same as in the smooth channel. Analysis of the interaction of the groove patterns on both walls demonstrates that the converging–diverging configuration results in the greatest increase in discharge while the wavy channel configuration results in a reduction in discharge.

Key words: drag reduction, flow control, turbulent flows

---

1. Introduction

In wall-bounded flows, power must be supplied to the flow in order to overcome dissipation by means of viscous and pressure drag. Increasing energy costs motivate the search for methods to reduce the power consumption and one way to achieve this goal is to reduce drag. Techniques resulting in the reduction of pressure drag are well established while methods that result in the reduction of friction drag are still being actively researched.

† Email address for correspondence: yuchen1986sg@gmail.com

It is well known that turbulent flows have higher skin friction than laminar flows and, thus, one of the popular drag-reducing techniques relies on the delay of the laminar–turbulent transition. Once the turbulent flow has been established, its structure can be rearranged using either passive or active devices with the hope that the new flow will be characterized by a smaller skin friction.

Since the beginning of modern fluid mechanics, it has been commonly believed that the drag on a smooth surface is always lower than that on a rough surface (Hagen 1854; Darcy 1857; Nikuradse 1933; Moody 1944). This is actually not the case, as documented through the development of special drag-reducing surface topographies; see a recent review in García-Mayoral & Jiménez (2011). The advantage of such topographies is in the passive character of the drag reduction which eliminates the energy costs associated with the use of active techniques (Choi, Jukes & Whalley 2011; Quadrio 2011). The physics of turbulent drag reduction is well summarized by Kim (2011).

One of the early passive methods of drag reduction was the large eddy break up (LEBU) method (Savill & Mumford 1988). This method usually employs small flat or airfoil shaped ribbons within the boundary layer. The wake behind such ribbons interacts with the turbulent boundary layer and suppresses the velocity normal to the wall (Balakumar & Widnall 1986; Graham 1998), resulting in a reduction in turbulent motion and skin friction immediately downstream of the devices. The drag reduction is up to 40 % as reported by Sahlin, Johansson & Alfredsson (1988), however there is a large spread and doubt in the drag reduction value due to the difficulty and inaccuracies of indirect measuring methods at relatively low Reynolds numbers (Savill & Mumford 1988). In addition, drag reduction at practically high Reynolds numbers seems implausible as LEBU devices reduce skin friction via breaking up the large-scale motions whose size becomes much smaller than the devices. This is supported by the direct force measurements conducted by Sahlin, Alfredsson & Johansson (1986), Sahlin *et al.* (1988) at Reynolds numbers up to 260 000.

Nature provides numerous examples of special drag-reducing surface topographies. Shark (superorder *Selachimorpha*) is one of the fastest swimming fish, whose speed can exceed 40–50 km h^{-1} (the 'shortfin mako shark' and the 'great white shark') during hunting. Microscopic examination of shark skin showed that it consists of small jagged and overlapping scales with a valley/ridge structure (denticle) in the flow direction. The scales are believed to disrupt the turbulent flow structures and in this manner they reduce the drag (Bechert, Bruse & Hage 2000; Dean & Bhushan 2010). Riblets, inspired by the shark skin, have the form of streamwise microgrooves and represent one of the well-known skin-friction reducing methods (Walsh 1980, 1983). The structure of riblets is different from shark skin, as the former has a continuous geometry while the latter is discrete in the streamwise direction. Riblets generally have two types of cross-section: wedge-like and blade-like (see Sudo *et al.* 2002). The height and spacing expressed in terms of wall units for the 'wedge' or 'blade' are approximately 10–30. It is generally accepted that the highest drag reduction that can be achieved in turbulent channel flow by riblets is approximately 7 %–9 % (Bechert *et al.* 1997; Itoh *et al.* 2006). The direct numerical simulations of Choi, Moin & Kim (1993) demonstrated that the drag reduction is achieved by depressing the velocity and vorticity fluctuations as well as the Reynolds stresses. See also Bechert & Bartenwerfer (1989) and Choi (1989).

Sirovich & Karlsson (1997) employed randomly patterned 'V' protrusions and experimentally found an approximately 10 % drag reduction in turbulent channel flow ($15\,000 < Re_{2H} < 40\,000$) as compared to a smooth channel. The experimental and

numerical results obtained by Sagong *et al.* (2008), however, showed that the drag on randomly patterned 'V' protrusions is increased by 0 %–15 %. The disagreement among researchers as to whether 'V' protrusions induce drag reduction led Chen, Chew & Khoo (2010) to conduct numerical simulations for Reynolds numbers $10\,000 < Re_{2H} < 40\,000$. Their results showed that neither the random nor aligned 'V' protrusions can reduce drag in a fully developed turbulent channel flow.

Another alternative is offered by the so-called super-hydrophobic effect (Rothstein 2010) which results from a combination of the hydrophobicity of the liquid and surface material and surface topography. When a super-hydrophobic surface is submerged inside a liquid, gas bubbles become trapped in surface micro-pores effectively reducing the shear stress experienced by the liquid, as shear between the liquid and the solid is replaced by shear between the liquid and the gas, with the research being inspired by the unique water-repellent properties of the lotus leaf (Barthlott & Neinhuis 1997). The drag reducing abilities can be increased by correctly shaping the surface pores/roughness (Samaha, Tafreshi & Gad-el Hak 2011) and by increasing hydrophobicity through changes in surface chemistry (Gao & McCarthy 2006; Quéré 2008; Reyssat, Yeomans & Quéré 2008; Zhang *et al.* 2008; Zhou *et al.* 2011). While laminar drag reduction due to the super-hydrophobic effect is well documented (Ou, Perot & Rothstein 2004; Ou & Rothstein 2005; Joseph *et al.* 2006; Truesdell *et al.* 2006), techniques which rely on this effect to reduce turbulent drag are still being developed (Daniello, Waterhouse & Rothstein 2009; Martell, Perot & Rothstein 2009; Park, Park & Kim 2013).

Dimpled surfaces, which were first designed and have been studied extensively for heat transfer enhancement (Burgess, Oliveira & Ligrani 2003), may also have the potential to reduce drag (Alekseev *et al.* 1998). Conflicting views on their drag reduction capability are reported; some studies (Alekseev *et al.* 1998; Veldhuis & Vervoort 2009) reported dramatic drag reduction even up to 10%–20 % compared to flat surfaces, while others (Lienhart, Breuer & Köksoy 2008; Tay, Khoo & Chew 2015) reported little (approximately 3 %) to no drag reduction in both external and internal turbulent flow. Tay *et al.* (2015) revealed that the turbulent motion on the small scales is suppressed by the streamwise vorticity generated on the dimpled surfaces, leading to the reduction of turbulent skin friction. It was also shown that, although increasing dimple depth further reduces skin friction, the net drag reduction may drop because of the significant increase in form drag due to the flow separation.

Besides the three-dimensional dimples, another macro-scale device is represented by two-dimensional grooves in channel flow. In order to examine the drag over such surfaces, Mohammadi & Floryan (2013*b*) investigated such grooves of arbitrary shape with an arbitrary orientation in laminar flow. It was found that transverse grooves produce the highest drag while longitudinal grooves produce the lowest drag. Drag reduction was reported for longitudinal grooves with long wavelengths, in spite of an increase in the wetted surface area. This reduction was attributed to the redistribution of the mass flow, with the largest mass flow taking place in the widest channel opening. It was found that short-wavelength grooves increase the drag when compared to the smooth channel. A detailed study of grooves of various shapes can be found in Mohammadi & Floryan (2015). Moradi & Floryan (2013) have shown that similar grooves reduce laminar drag in an annulus flow. It is possible that the same grooves may be able to reduce turbulent drag.

Several active methods have been developed for drag reduction and they are briefly reviewed for completeness. Spanwise in-plane wall oscillations have the potential for up to 40 % drag reduction (Quadrio 2011). The creation of such waves using plasma

actuation is discussed in Choi *et al.* (2011). Considering the energy needed to drive the oscillation, the maximum net energy saving is approximately 5 %–10 %. Upstream travelling waves produced by suction/blowing can reduce the turbulent drag to below that for the laminar flow (Min *et al.* 2006). A similar effect is achieved by elastic wall deformation waves (Hoepffner & Fukagata 2009). Schoppa & Hussain (1998) showed that counter-rotating streamwise vortices produced by colliding wall jets were able to reduce drag by 20 %. Iuso *et al.* (2002) experimentally showed that counter-rotating vortex pairs, which are generated by jet injection, reduce the mean skin friction by 15 %.

Though considerable effort has been expended to develop various potential drag-reducing techniques, techniques that are readily applicable in engineering practice are yet to be identified. Riblets, 'V' protrusions and super-hydrophobic surfaces containing micro-scale structures are difficult to manufacture and maintain. Active methods need additional power, which reduces their efficiency and creates hardware needs which can be difficult to overcome. Thus, there is a need to design a novel device which is passive (no additional energy input), has a macro-scale format (easy to manufacture and maintain) and still has a high level of drag reduction (no less than that of riblets).

Considering the advantages of macro-scale surface modifications over micro-scale modifications (e.g. riblets, superhydrophobic surfaces, etc), the objective of this analysis is to carry out a detailed investigation of turbulent flows in channels with surfaces modified with longitudinal grooves of arbitrary shape and wavelength. It is known that grooves with long wavelengths are able to reduce the laminar drag. Our intent is to determine if there are classes of such grooves which are able to reduce the turbulent drag, to explore in detail the performance of such grooves and to identify the possible mechanism(s) responsible for the drag reduction. The drag-reducing potential is measured by comparing the discharge through the grooved channel with the discharge through a smooth channel when both channels are exposed to the same pressure gradient.

This paper is organized as follows. The channel geometry and the governing equations are introduced in §2. The analytical results for the laminar flows are presented in §3. Turbulent flows are investigated numerically in §4. The concluding remarks are provided in §5.

2. Problem formulation

2.1. *Channel geometry*

Consider fluid flow driven by a known pressure gradient through a channel extending to $\pm\infty$ in the *x*-direction bounded by walls fitted with straight grooves parallel to the flow direction (see figure 1) and of arbitrary shape in the spanwise *z*-direction. The channel geometry is described using Fourier expansions of the form

$$y_L(z) = -1 + \sum_{m=-N_A}^{m=N_A} H_L^{(m)} e^{im\alpha z}, \qquad (2.1a)$$

$$y_U(z) = 1 + \sum_{m=-N_A}^{m=N_A} H_U^{(m)} e^{im\alpha z}, \qquad (2.1b)$$

where the subscripts *L* and *U* refer to the lower and upper walls, respectively, $\lambda = 2\pi/\alpha$ denotes the groove wavelength, α stands for the groove wavenumber,
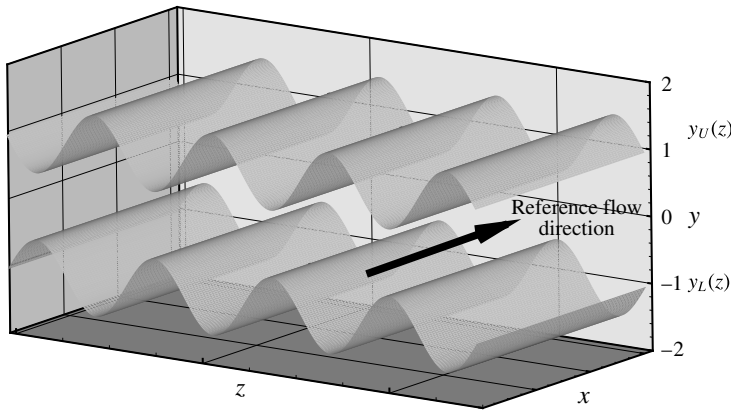
FIGURE 1. Sketch of the flow configuration.

$H_L^{(m)} = H_L^{(-m)**}$ and $H_U^{(m)} = H_U^{(-m)**}$ are the reality conditions, double stars denote the complex conjugates, N_A represents the number of Fourier modes required to describe the geometry and the half-channel height H^* of the reference smooth channel has been used as the length scale. The objective of this analysis is to describe the effects of the flow modulations on the channel discharge and, accordingly, it is assumed that the mean openings of the grooved and the reference smooth channels are the same, i.e. $H_L^{(0)} = H_U^{(0)} = 0$.

2.2. *Field equations*

It is assumed that the introduction of the grooves does not affect the mean streamwise pressure gradient and, thus, the pressure is represented as $p(x, y, z, t) = -x + p'(x, y, z, t) + \text{const}$. The discharge is, however, affected and its evaluation requires solving the field equations of the form

$$\frac{\partial u}{\partial x} + \frac{\partial v}{\partial y} + \frac{\partial w}{\partial z} = 0, \tag{2.2a}$$

$$\frac{\partial u}{\partial t} + \frac{\partial(uu)}{\partial x} + \frac{\partial(uv)}{\partial y} + \frac{\partial(uw)}{\partial z} = 1 - \frac{\partial p'}{\partial x} + \frac{1}{Re_\tau}\left(\frac{\partial^2 u}{\partial x^2} + \frac{\partial^2 u}{\partial y^2} + \frac{\partial^2 u}{\partial z^2}\right), \tag{2.2b}$$

$$\frac{\partial v}{\partial t} + \frac{\partial(vu)}{\partial x} + \frac{\partial(vv)}{\partial y} + \frac{\partial(vw)}{\partial z} = -\frac{\partial p'}{\partial y} + \frac{1}{Re_\tau}\left(\frac{\partial^2 v}{\partial x^2} + \frac{\partial^2 v}{\partial y^2} + \frac{\partial^2 v}{\partial z^2}\right), \tag{2.2c}$$

$$\frac{\partial w}{\partial t} + \frac{\partial(wu)}{\partial x} + \frac{\partial(wv)}{\partial y} + \frac{\partial(ww)}{\partial z} = -\frac{\partial p'}{\partial z} + \frac{1}{Re_\tau}\left(\frac{\partial^2 w}{\partial x^2} + \frac{\partial^2 w}{\partial y^2} + \frac{\partial^2 w}{\partial z^2}\right), \tag{2.2d}$$

where (u, v, w) are the components of the velocity vector in the (x, y, z) directions, respectively, the friction velocity defined as $u_\tau^* = \sqrt{\beta^* H^*/\rho^*}$ is used as the velocity scale, β^* stands for the mean pressure gradient in the x-direction, ρ^* denotes density, H^* is the mean channel half-height, H^*/u_τ^* is used as the time scale, $\rho^* u_\tau^{*2}$ is used as the pressure scale and $Re_\tau = u_\tau^* H^*/\nu^*$ is the friction Reynolds number where ν^* denotes the kinematic viscosity. For interpretation purposes we shall also need the Reynolds number based on the bulk fluid velocity U_b^* and the full height of the reference smooth channel defined as $Re_{2H} = U_b^* 2H^*/\nu^*$ where $U_b^* = \iint U^* \, dA^* / \iint dA^*$

with A^* standing for the channel cross-sectional area associated with one groove wavelength. In the above, stars denote the dimensional quantities. System (2.2) is subject to the homogeneous boundary conditions of the form

$$u = v = w = 0 \quad \text{at } y = y_L(z) \quad \text{and} \quad y = y_U(z). \tag{2.3}$$

The discharge is determined during the post-processing according to the formula

$$Q(t, x)|_{mean} = \left[\frac{1}{2\pi/\alpha} \int_{z=0}^{z=2\pi/\alpha} \int_{y=y_L(z)}^{y=y_U(z)} u(y, z) \, \mathrm{d}y \, \mathrm{d}z \right]\Bigg|_{mean}. \tag{2.4}$$

An increase of Q_{mean} above the reference discharge created by the same pressure gradient in the smooth channel demonstrates an increase in the effectiveness of the flow system, or effective drag reduction.

3. Laminar channel flow

We begin the analysis with the laminar flow. It has been demonstrated that long-wavelength grooves are able to reduce the pressure gradient which is required to drive a prescribed discharge (Mohammadi & Floryan 2013*a*,*b*; Moradi & Floryan 2013). The same grooves increase the discharge through the channel if the same pressure gradient is applied to both the smooth as well as the grooved channels. We shall review these results before proceeding to the analysis of turbulent flows. We shall also demonstrate existence of an analytic solution which is valid for the range of parameters where the grooves are able to increase the flow discharge.

Equations (2.2) can be reduced to the form

$$\Delta u = -Re_\tau, \tag{3.1}$$

where $\Delta = \partial^2/\partial y^2 + \partial^2/\partial z^2$. The Reynolds number is a multiplicative factor, which can be scaled out by defining a new velocity u_r

$$u = u_r Re_\tau, \tag{3.2}$$

and leading to the field equation of the form

$$\Delta u_r = -1. \tag{3.3}$$

The boundary conditions take the form

$$u_r = 0 \quad \text{at } y = y_L(z) \quad \text{and} \quad y = y_U(z). \tag{3.4}$$

So the solution of u_r is independent of Reynolds number for laminar flow.

The solution in the case of smooth channel has the form

$$u_r = \frac{1 - y^2}{2}, \quad Q_0 = \frac{2}{3} Re_\tau \tag{3.5a,b}$$

and defines the reference point for the determination of changes in the system performance.

Equations (3.3)–(3.4) can be solved using expansions in terms of the groove amplitude. To demonstrate the construction and range of validity of such solutions, we shall consider a channel with grooves on both walls with the channel shape described by one Fourier mode, i.e.

$$y_L = -1 - \frac{S}{2}\sin(\alpha z), \quad y_U = 1 + \frac{S}{2}\sin(\alpha z), \tag{3.6a,b}$$

where S is the amplitude of the corrugation non-dimensionalized with H^*.

This particular geometry represents a reduced geometry model of grooves with arbitrary shapes (Mohammadi & Floryan 2013*b*; Moradi & Floryan 2013).

Assume the solution to be of the form

$$u_r(y, z) = u_r^{(0)} + S u_r^{(1)} + S^2 u_r^{(2)} + S^3 u_r^{(3)} + \cdots. \tag{3.7}$$

By substituting into (3.3)–(3.4), transferring boundary conditions to $y = \pm 1$ and collecting terms of the same order of magnitude, we arrive at the following set of problems:

$$O(S^0): \Delta u_r^{(0)} = -1, \quad u_r^{(0)}(\pm 1, z) = 0, \tag{3.8}$$

$$O(S^1): \Delta u_r^{(1)} = 0, \quad u_r^{(1)}(\pm 1, z) = \mp \tfrac{1}{2} u_{r,y}^{(0)}(\pm 1, z)\sin(\alpha z), \tag{3.9}$$

$$O(S^2): \Delta u_r^{(2)} = 0, \quad u_r^{(2)}(\pm 1, z) = \mp \tfrac{1}{2} u_{r,y}^{(1)}(\pm 1, z)\sin(\alpha z) - \tfrac{1}{8} u_{r,yy}^{(0)}(\pm 1, z)\sin^2(\alpha z), \tag{3.10}$$

$$O(S^3): \Delta u_r^{(3)} = 0, \quad u_r^{(3)}(\pm 1, z) = \mp \tfrac{1}{2} u_{r,y}^{(2)}(\pm 1, z)\sin(\alpha z) - \tfrac{1}{8} u_{r,yy}^{(1)}(\pm 1, z)\sin^2(\alpha z)$$
$$\mp \tfrac{1}{48} u_{r,yyy}^{(0)}(\pm 1, z)\sin^3(\alpha z). \tag{3.11}$$

Their solutions have the form

$$u_r^{(0)} = \frac{1 - y^2}{2}, \tag{3.12}$$

$$u_r^{(1)} = \frac{\cosh(\alpha y)\sin(\alpha z)}{2\cosh(\alpha)}, \tag{3.13}$$

$$u_r^{(2)} = \frac{[1 - 2\alpha \tanh(\alpha)]}{16}\left[1 - \frac{\cosh(2\alpha y)}{\cosh(2\alpha)}\cos(2\alpha z)\right], \tag{3.14}$$

$$u_r^{(3)} = \frac{\alpha\{-3\alpha + [-2 + 4\alpha \tanh(\alpha)]\tanh(2\alpha)\}}{64}\frac{\cosh(\alpha y)}{\cosh(\alpha)}\sin(\alpha z)$$
$$+ \frac{\alpha\{\alpha + [2 - 4\alpha \tanh(\alpha)]\tanh(2\alpha)\}}{64}\frac{\cosh(3\alpha y)}{\cosh(3\alpha)}\sin(3\alpha z). \tag{3.15}$$

Evaluation of the discharge results in the following expression

$$\frac{Q(\alpha, S)}{Re_\tau} = \frac{\alpha}{2\pi}\int_\Omega u_r \, dy \, dz = \frac{\alpha}{2\pi}\left(\int u_r^{(0)} + S\int u_r^{(1)} + S^2\int u_r^{(2)} + S^3\int u_r^{(3)} + \cdots\right)$$
$$= \frac{2}{3} + \frac{S}{\alpha}I_1\left(\frac{\alpha S}{2}\right) - \frac{\alpha S^2 \tanh(\alpha)}{4}$$
$$+ \frac{\alpha S^4[1 - 2\alpha \tanh(\alpha)]\tanh(2\alpha)}{128}\left(1 + \frac{\alpha^2 S^2}{12}\right)$$

$$+ \frac{S^3\{-3\alpha + [-2 + 4\alpha \tanh(\alpha)] \tanh(2\alpha)\}}{32} I_1 \left(\frac{\alpha S}{2} \right)$$

$$- \frac{3\alpha^3 S^6 \{\alpha + [2 - 4\alpha \tanh(\alpha)] \tanh(2\alpha)\}}{4096} \left(1 + \frac{9}{64} \alpha^2 S^2 \right)$$

$$+ O(\alpha^6 S^8) + O(\alpha S^5), \tag{3.16}$$

where I_1 is the first-order modified Bessel function of the first kind. This solution is valid for $\alpha S \ll 1$. A similar procedure for grooves located on one wall only results in a channel geometry of the form

$$y_L = -1 - \frac{S}{2} \sin(\alpha z), \quad y_U = 1. \tag{3.17a,b}$$

This leads to a solution of the form

$$u_r^{(0)} = \frac{1 - y^2}{2}, \tag{3.18}$$

$$u_r^{(1)} = \frac{\sin(\alpha z)}{4} \left[\frac{\cosh(\alpha y)}{\cosh(\alpha)} + \frac{\sinh(\alpha y)}{\sinh(\alpha)} \right], \tag{3.19}$$

$$u_r^{(2)} = \frac{[1 - 2\alpha \, \text{ctanh}(2\alpha)]}{16} \left\{ \frac{y + 1}{2} \right.$$
$$\left. - \frac{1}{2} \left[\frac{\cosh(2\alpha y)}{\cosh(2\alpha)} + \frac{\sinh(2\alpha y)}{\sinh(2\alpha)} \right] \cos(2\alpha z) \right\}, \tag{3.20}$$

$$u_r^{(3)} = \widehat{C_1} \left[\frac{\cosh(\alpha y)}{\cosh(\alpha)} + \frac{\sinh(\alpha y)}{\sinh(\alpha)} \right] \sin(\alpha z) \tag{3.21}$$

$$+ \widehat{C_2} \left[\frac{\cosh(3\alpha y)}{\cosh(3\alpha)} + \frac{\sinh(3\alpha y)}{\sinh(3\alpha)} \right] \sin(3\alpha z), \tag{3.22}$$

where

$$\left. \begin{aligned} \widehat{C_1} &= -\frac{\{3\alpha^2 + [1 - 2\alpha \, \text{ctanh}(2\alpha)][1 + 2\alpha \, \text{ctanh}(4\alpha)]\}}{128}, \\ \widehat{C_2} &= \frac{\alpha\{\alpha + 2[1 - 2\alpha \, \text{ctanh}(2\alpha)]\text{ctanh}(4\alpha)\}}{128}. \end{aligned} \right\} \tag{3.23}$$

The discharge can be evaluated as

$$\frac{Q(\alpha, S)}{Re_\tau} = \frac{\alpha}{2\pi} \int_\Omega u_r \, dy \, dz = \frac{\alpha}{2\pi} \left(\int u_r^{(0)} + S \int u_r^{(1)} + S^2 \int u_r^{(2)} + S^3 \int u_r^{(3)} + \cdots \right)$$

$$= \frac{2}{3} + \frac{Re_\tau S}{2\alpha} I_1 \left(\frac{\alpha S}{2} \right) - \frac{Re_\tau \alpha S^2 \, \text{ctanh}(2\alpha)}{8}$$

$$+ \frac{\alpha S^4 [1 - 2\alpha \, \text{ctanh}(2\alpha)]}{512}$$

$$+ \frac{\alpha S^4 [1 - 2\alpha \, \text{ctanh}(2\alpha)]\text{ctanh}(4\alpha)}{256} \left(1 + \frac{1}{12} \alpha^2 S^2 \right)$$

$$+ \frac{2\widehat{C_1}S^3}{\alpha} I_1\left(\frac{\alpha S}{2}\right) + \widehat{C_2}\alpha^2 S^6 \left[\frac{3}{64} + \frac{27}{4096}\alpha^2 S^2\right]$$
$$+ O(\alpha^6 S^8) + O(\alpha S^5). \tag{3.24}$$

One may note that the ratio of the discharges in the smooth and corrugated channels Q/Q_0 is independent of Re_τ. The normalized discharge difference defined as

$$\Delta Q(\alpha, S) = \frac{Q - Q_0}{Q_0} = \frac{Q}{Q_0} - 1, \tag{3.25}$$

can be used to evaluate the system effectiveness with positive ΔQ indicating improvements. It is simple to show that

$$\lim_{S \to 0} \Delta Q = 0, \tag{3.26}$$

$$\lim_{\alpha \to 0} \Delta Q = \begin{cases} \dfrac{3S^2}{8} & \text{for channels with both walls grooved} \\ \dfrac{3S^2}{32} & \text{for channels with a single grooved wall.} \end{cases} \tag{3.27}$$

One can also show that

$$\max \Delta Q = \lim_{\alpha \to 0, S \to 2} \Delta Q = \frac{3}{2}, \tag{3.28}$$

which demonstrates that both a reduction of α as well as an increase of S can lead to an increase in the discharge. The dependence of ΔQ on α and S, as illustrated in figure 2, demonstrates the existence of a critical wavenumber α_c which separates grooves which improve the system performance from those which compromise the system performance, in agreement with the prediction of Mohammadi & Floryan (2013a,b). According to Moradi & Floryan (2013): $\alpha_c \approx 1.2$ for channels with grooves on both walls and $\alpha_c \approx 0.96$ for channels with grooves on one wall. Reduction of α increases the system efficiency but an excessive reduction is not helpful as ΔQ very rapidly reaches its asymptotic state and an excessive reduction of α results in negligible improvements. Although one may expect the increase in discharge to double with two corrugated walls (versus just one corrugated wall), it in fact becomes approximately four times as large due to the nonlinear interaction between flows induced by both corrugated walls.

Figure 2 also displays results determined numerically using a spectrally accurate solution (Mohammadi & Floryan 2013b). It can be seen that the theoretical predictions match very well with the numerical results for $\alpha S < 1$ and begin to diverge for larger α despite using several terms in the boundary conditions transfer procedure. This is in agreement with the results of Cabal, Szumbarski & Floryan (2001).

Since the streamwise pressure gradient is assumed to be the same with and without grooves, the total drag experienced by the moving fluid remains the same in both cases. Any increase in the discharge indicates the reduction of wall friction coefficient as the fluid velocity must increase in order to create the friction required to balance the pressure gradient. Introducing grooves increases the wetted area and, thus, greater discharge implies flow rearrangements which sufficiently reduce the wall friction so that the total drag remains the same in spite of the increase of the wetted area.

Figure 3 illustrates the velocity in the (y, z) channel cross-section. The results in figure 3(a) are for $\alpha = 0.5 < \alpha_c$ and correspond to an increase in discharge, while
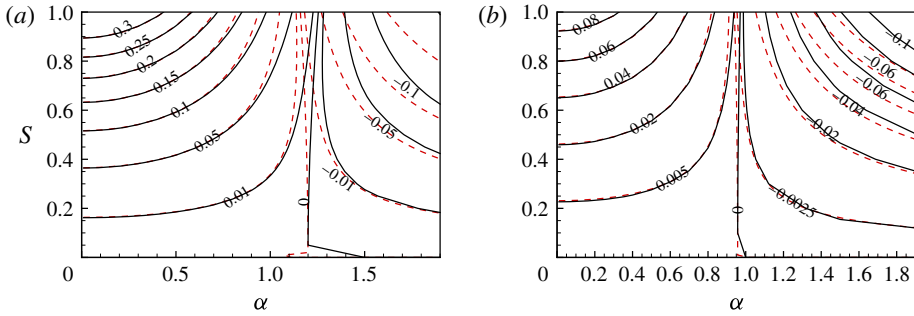
FIGURE 2. (Colour online) Variations of ΔQ as a function of the groove wavenumber and the amplitude in a channel with grooves on both walls (*a*) and on one wall only (*b*). Solid lines correspond to the analytical solution discussed above and dashed lines correspond to a numerical solution determined using the method described in Mohammadi & Floryan (2013*b*).
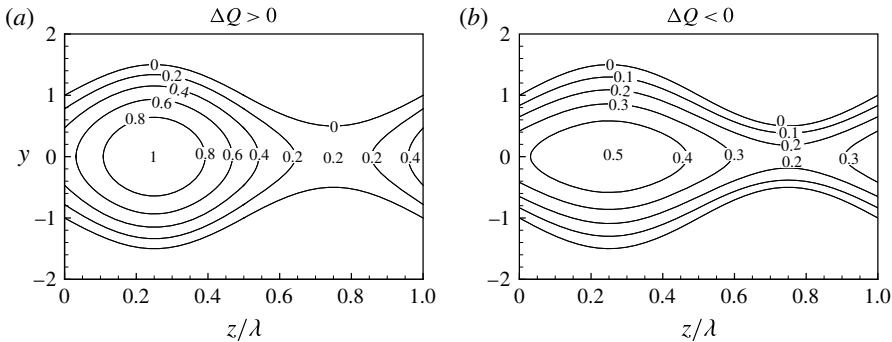

FIGURE 3. Streamwise velocity u_r in the y–z plane: (*a*) $\alpha = 0.5$, $S = 1$; (*b*) $\alpha = 2$, $S = 1$.

results in figure 3(*a*) for $\alpha = 2 > \alpha_c$ correspond to a decrease in discharge. The formation of stream tubes of high velocity fluid is visible in both cases, however, the maximum velocity in the former case approaches 1 while in the latter case it reaches only approximately 0.5, which is the same as the maximum velocity in the smooth channel. It is then not surprising that the discharge increases in the former case while it decreases in the latter.

The drag is generated only by friction. The spanwise distribution of the normalized x-component of the shear stress Sm/Sm_0 is illustrated in figure 4. Here Sm_0 denotes the reference skin friction (skin friction in the smooth channel) and Sm stands for the actual skin friction, i.e. the x-component of the local shear stress acting on the channel wall per unit wall is projected on the x–z plane, and is defined as

$$Sm = \frac{\partial u}{\partial y} - \frac{\partial u}{\partial z}\frac{\mathrm{d}y_L}{\mathrm{d}z}. \tag{3.29}$$

The reader may note that Sm integrated in the z-direction over one groove wavelength always results in the same value regardless of the groove shape; this value is equal in the average shear as the shear drag must balance the pressure drop. It can be seen that when $\alpha = 0.5 < \alpha_c$ (increased discharge), $Sm/Sm_0 > 1$ in the wide portion

FIGURE 4. (Colour online) Normalized shear acting on the fluid at the lower surface.
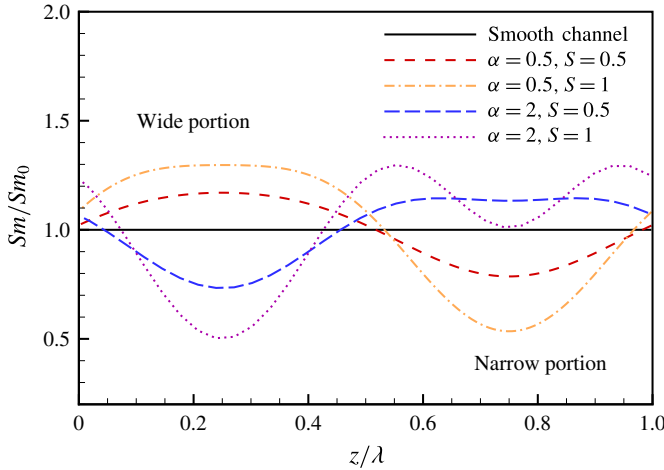
and $Sm/Sm_0 < 1$ in the narrow portion of the channel. Conversely, when $\alpha = 2 > \alpha_c$ (reduced discharge), $Sm/Sm_0 < 1$ in the wide portion and $Sm/Sm_0 > 1$ in the narrow portion of channel. It can be concluded that the increase in discharge associated with the presence of the grooves results from the rearrangement of the velocity field which leads to a decrease in the wall shear stress. Since the pressure gradient remains the same with and without grooves, the flow accelerates in the former case until the additional shear is able to balance the applied pressure gradient, resulting in an increase in discharge.

4. Turbulent flow

4.1. *Methodology*

The field equations (2.2) are solved in a computational box formed by the walls and $x \in (0, L)$, $z \in (0, W)$. The minimum size of the box has been determined through numerical testing to be discussed later in this presentation. The relevant boundary conditions consist of (2.3) and

$$u(0, y, z, t) = u(L, y, z, t), \; v(0, y, z, t) = v(L, y, z, t), \; w(0, y, z, t) = w(L, y, z, t), \quad (4.1a)$$

$$u(x, y, 0, t) = u(x, y, W, t), \; v(x, y, 0, t) = v(x, y, W, t), \; w(x, y, 0, t) = w(x, y, W, t),$$
$$(4.1b)$$

where (4.1) expresses the periodicity conditions in the x- and z-directions.

The results are presented as sums of the mean value and fluctuations defined as

$$G = \lim_{T \to \infty} \frac{\int_0^T g \, dt}{T}, \quad g' = g - G, \quad \langle g'h' \rangle = \lim_{T \to \infty} \frac{\int_0^T g'h' \, dt}{T}, \quad (4.2a\text{--}c)$$

where G stands for the mean value of any flow quantity (e.g. u, v, w, p), T denotes the sampling time, g' denotes the fluctuating component and $\langle g'h' \rangle$ denotes statistical variables such as Reynolds stress $\langle u'v' \rangle$. In the computations, $t = 0$–40 is treated as a

transient period required for the flow to reach a statistically steady state. Data from $t = 40$–80 are used to determine averages (such as U, V, W). During the sampling time, i.e. from $t = 40$ to $t = 80$, the fluid can travel in the streamwise direction for approximately 60 length units (distance equal to 30 channel heights). Flow data for $t = 80$–120 are used to evaluate statistical quantities such as Reynolds stress and to carry out turbulent quadrant analysis.

It is useful to introduce scales used in the description of turbulent flows. The ratio of the channel half-height and the friction velocity defines the time scale and the dimensionless time expressed using this time scale is denoted as t. Velocity scaled with the friction velocity u_τ^* is typically denoted as U^+ but we shall continue using the notation introduced in the previous section. The viscous length scale $l^* = \nu^*/u_\tau^*$ leads to the dimensionless quantities to be identified with the superscript $^+$. In particular, we shall move the origin of the y^+-axis to the lower wall, e.g.

$$
\begin{aligned}
y^+ &= \frac{y_w^*}{l^*} \\
&= \frac{y^* + y_L^*}{l^*} \\
&= \frac{y^* + y_L^*}{H^*} \frac{u_\tau^* H^*}{\nu^*} \\
&= (y + y_L) Re_\tau,
\end{aligned}
\tag{4.3}
$$

where y_w^* refers to the dimensional distance from the wall. The relation between the dimensionless coordinates in the other two directions can be similarly determined, e.g. $x^+ = x Re_\tau$ and $z^+ = z Re_\tau$.

The statistical quantities (e.g. mean velocity, turbulent kinetic energy) are typically averaged in the horizontal plane (e.g. averaged in both the streamwise and spanwise directions; (Kim, Moin & Moser 1987)). We shall use streamwise only averaging for grooved channels as plane averaging eliminates the groove induced modulations. We shall use horizontal averaging for the smooth channel unless explicitly stated otherwise, following Quadrio, Floryan & Luchini (2007).

4.1.1. *Direct numerical simulation*

The field equations (2.2) subject to boundary conditions (2.3) and (4.1) have been solved as an initial value problem through direct numerical solution (DNS) of the time-dependent problem. One can use for spatial discretization either spectral (Kim *et al.* 1987; Moser, Kim & Mansour 1999) or finite-volume (Wang, Yeo & Khoo 2006) methods. The spectral methods are difficult to implement in domains with complex boundaries and thus we shall use the finite-volume method. Second-order implicit time integration and second-order central spatial differencing have been used. The standard multi-grid algorithm (Wesseling & Oosterlee 2001) has been used for the discretized pressure correction equation and the discretized momentum equation with the three-dimensional (3-D) alternating direction implicit (ADI) solver (Douglas 1955; Chang, Chow & Chang 1991) used as the smoother. The solver has been parallelized using domain decomposition concepts coupled with MPI (message passing interface). The interface communications between the adjacent computational blocks has been handled using ghost volumes with one level of overlap.

The algorithm has been validated using simulations of turbulent flow in a smooth channel at $Re_\tau = 180$ with a computational box of size $L = 2\pi$ ($L^+ \approx 1131$) and width $W = 2\pi$ ($W^+ \approx 1131$). The friction coefficient C_{f0} has been used as the test

Mesh	Cells number	Δx^+	Δz^+	Δy^+_{min}	Δt	Re_{2H}	C_{f0}/C_f^0 (%)
1	$64 \times 64 \times 64$	17.671	17.671	0.5006	0.004	5929.3	90.91
2	$64 \times 64 \times 64$	17.671	17.671	0.5006	0.002	5928.1	91.35
3	$96 \times 96 \times 96$	11.781	11.781	0.3572	0.002	5861.2	95.43
4	$128 \times 128 \times 128$	8.836	8.836	0.2368	0.004	5830.4	97.74
5	$128 \times 128 \times 128$	8.836	8.836	0.2368	0.002	5829.8	97.95
6	$128 \times 196 \times 128$	8.836	8.836	0.1254	0.002	5827.5	99.91

TABLE 1. Mesh convergence study for the DNS method.

quantity and has been compared with the empirical friction coefficient C_f^0 taken from the Petukhov & Gielinski correlation (Incropera & DeWitt 2002), i.e.

$$C_f^0 = [1.58 \ln(Re_{2H}) - 2.185]^{-2}, \quad 1500 \leqslant Re_{2H} \leqslant 2.5 \times 10^6. \quad (4.4)$$

Here, the friction coefficient is defined as

$$C_f = \frac{\tau_w^*}{\frac{1}{2}\rho^* U_b^{*2}} = \frac{2}{U_b^2}, \quad (4.5)$$

where, τ_w^* is the dimensional skin-friction stress and U_b represents the non-dimensional bulk fluid velocity U_b^*/u_τ. Friction coefficients C_{f0} with subscript '$_0$' are calculated from numerical simulations while C_f^0 with superscript '^{0}' are empirical results given by (4.4).

A uniform grid has been used in the *x*- and *z*-directions and a stretched grid based on the hyperbolic tangent has been used in the *y*-direction (Moin & Kim 1982; Abe, Kawamura & Matsuo 2001). Results summarized in table 1 demonstrate that $C_{f0}/C_f^0 \to 1$ as the grid is refined, as expected. It can be concluded that the grid 128^3 as well as the time step 0.002 provide sufficient accuracy. The reader may note that Re_{2H} is not imposed but has been computed after the statistically convergent state has been reached.

4.1.2. *Detached eddy simulation*

The detached eddy simulation (DES) model is a hybrid technique originally developed for turbulent flows with massive separation. It was first introduced by Spalart, Jou & Allmaras (1997) as a modification of the Spalart–Allmaras (S–A) model (Spalart & Allmaras 1992). The S–A model is a one-equation model for the eddy viscosity ν_T dependent on the distance to the closest wall d_w; d_w from the original S–A model has been replaced with $\tilde{d}$ defined as

$$\tilde{d} = \min(d_w, C_{DES}\Delta), \quad (4.6)$$

where C_{DES} is a parameter that controls the switch point between the near wall and far fields and Δ represents the largest grid spacing in all three directions, i.e. $\Delta = \max(\Delta x, \Delta y, \Delta z)$, resulting in the DES model. In the near-wall regions ($d_w < C_{DES}\Delta$), the DES model acts as the Reynolds average Navier–Stokes (RANS) model. Conversely, it behaves as the large eddy simulation (LES) model when $d_w > C_{DES}\Delta$. Overall, the grid resolution of DES is not as demanding as the pure LES approach, thereby reducing the cost of computations. The DES model has been

Mesh	Cell number	Δx^+	Δz^+	Δy^+_{min}	Re_{2H}	C_{f0}/C_f^0 (%)
1	$16 \times 64 \times 16$	70.686	70.686	0.5006	6856.8	90.8
2	$32 \times 64 \times 32$	35.343	35.343	0.5006	6432.8	85.6
3	$64 \times 64 \times 64$	17.671	17.671	0.5006	5927.5	91.2
4	$32 \times 128 \times 32$	35.343	35.343	0.2368	6440.3	84.5
5	$64 \times 128 \times 64$	17.671	17.671	0.2368	5932.4	94.3
6	$96 \times 128 \times 96$	11.781	11.781	0.2368	5860.7	95.1
7	$128 \times 128 \times 128$	8.836	8.836	0.2368	5829.2	95.4

TABLE 2. Mesh convergence study for the DES method.

Domain	Domain size	Re_{2H}	C_{f0}/C_f^0 (%)
1	$2\pi \times 2 \times \pi$	5923.8	93.8
2	$2\pi \times 2 \times 2\pi$	5932.4	94.3
3	$4\pi \times 2 \times \pi$	5898.5	93.9

TABLE 3. Study of the effects of the size of the computational box for the DES method.

used in this work with the constant C_{DES} taken as 0.65 (see Shur *et al.* 1999). It is a proper choice which ensures a narrow transition region between RANS and LES, resulting in accurate results from DES (Keating & Piomelli 2006). The convergence has been enhanced using modifications to the S–A model as described by Tu *et al.* (2009). The time step size and the spatial grid used in the DES algorithm are the same in the DNS.

A mesh resolution study for DES has been carried out in the same manner as for DNS. The results displayed in table 2 demonstrate that the grid $64 \times 128 \times 64$ provides sufficient accuracy. While the grid 128^3 provides greater accuracy, the potential gains are outweighed by the computational cost. As the primary objective of this study is to determine variations of the discharge as a function of the wall geometry, it has been concluded that the grid $64 \times 128 \times 64$ provides a good compromise between the cost and the desired accuracy.

The size of the computational box may affect the overall accuracy if this box is too small and thus unable to capture large coherent flow structures. Results of testing displayed in table 3 for three different computational boxes demonstrate that variations of (C_{f0}/C_f^0) are within 0.5 % and, thus, the smallest box is large enough to accurately reproduce the flow physics.

Next, the domain independence study is conducted to obtain the effects of spatial dimensions on capturing the relevant flow structures which may impact the calculated friction. The results of three different domain sizes are listed in table 3. The fact that the variations of the friction ratio (C_{f0}/C_f^0) are in the range of 0.5 % demonstrates the present results are fairly independent of the domain size.

4.1.3. *The mean velocity profile, the turbulent kinetic energy and the Reynolds stress*

The mean velocity profiles, the turbulent kinetic energy and the Reynolds stress determined using both DNS with grid 128^3 and DES with grid $64 \times 128 \times 64$ and a computational box ($2\pi \times 2 \times 2\pi$) as displayed in figure 5 demonstrate the consistency between DNS and DES. The mean velocity profiles match fairly well with those obtained by Moser *et al.* (1999), though the velocities given by DNS and DES
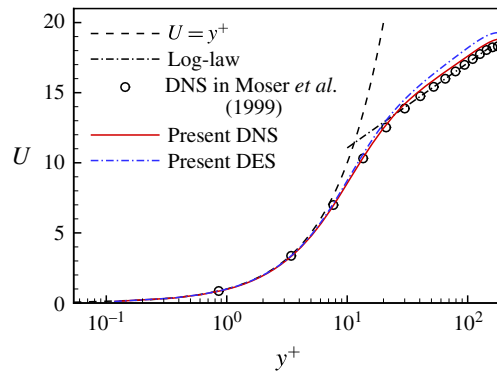
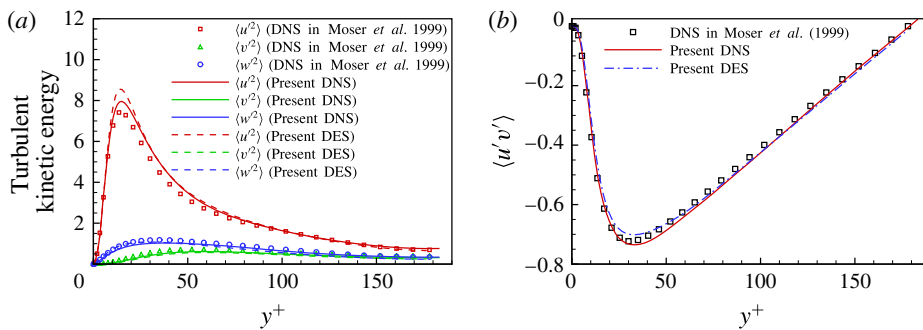FIGURE 5. (Colour online) Distribution of the mean velocity U in a smooth channel for $Re_\tau = 180$.

FIGURE 6. (Colour online) Distributions of the turbulent kinetic energy components (*a*) and the Reynolds stress $\langle u'v' \rangle$ (*b*) for $Re_\tau = 180$.

are slightly higher in the log-law region, leading to an underestimation of the drag coefficient (approximately 6 % for DES and 2 % for DNS). Figure 6 displays the turbulent kinetic energy components ($\langle u'^2 \rangle$, $\langle v'^2 \rangle$ and $\langle w'^2 \rangle$) and the Reynolds stress ($\langle u'v' \rangle$). Results produced using DES and DNS agree fairly well with those given by Moser *et al.* (1999) with the peak value of $\langle u'^2 \rangle$ given by DES and DNS being slightly higher than that of Moser *et al.* (1999) while the position of the peak at $y^+ = 15$ is captured correctly.

One can conclude that the DES and DNS results produced during code validation agree fairly well with the DNS results obtained by Moser *et al.* (1999); the minor differences are likely due to the lower spatial resolution of the finite-volume method (FVM). The FVM-based DNS/DES with the selected resolution may not provide the same level of accuracy as the spectral DNS method due to the possibly unresolved small-scale motions, which may lead to underestimation of the turbulent kinetic energy and the Reynolds stress herein. However, the bulk flow manipulation inside the corrugated channel is directly influenced by the cross-section shape (as opposed to the near-wall effect); the small-scale motions near the wall and its effects are not the main focus of the current study. In addition, the key features and trend of the turbulent flow like the drag coefficient, the velocity profile, the turbulent kinetic
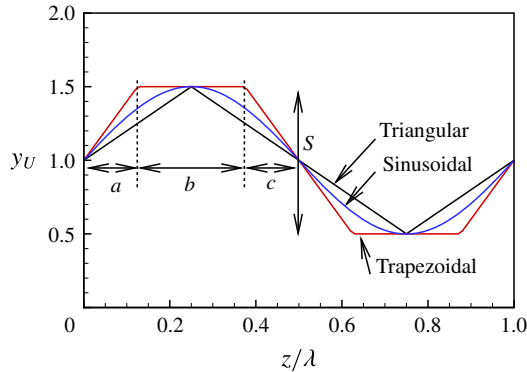
FIGURE 7. (Colour online) Sinusoidal, triangular and trapezoidal grooves used in the analysis.

ΔQ	DES (%)	DNS (%)
$\alpha = 0.5, \ S = 0.5$	1.29	0.98
$\alpha = 0.4, \ S = 1$	4.38	3.77
$\alpha = 0.25, \ S = 1$	6.72	6.43

TABLE 4. The difference of the discharge determined using the DES and DNS methods for $Re_\tau = 180$.

energy and the Reynolds stress, can be well reproduced using the finite-volume-based DES method and thus this method has been used in the study of corrugated channels.

4.2. *Validation of DES for turbulent flows in corrugated channels*

Tests carried out for flows in smooth channels demonstrated that DES provides accuracy similar to DNS. It remains to be demonstrated that both methods provide a similar accuracy for grooved channels. Results presented in table 4 show a discharge difference of less than 0.5 % between the methods which justifies the use of the more computationally efficient DES method.

4.3. *Reduced geometry model for turbulent channel flows*

It has been demonstrated that sinusoidal grooves play the role of the reduced geometry model for laminar flows (Mohammadi & Floryan 2013*b*; Moradi & Floryan 2013). We shall demonstrate that such grooves also represent the reduced geometry model in turbulent flows. We shall use triangular and trapezoidal grooves illustrated in figure 7 for this demonstration.

Table 5 displays results for groove wavenumber $\alpha = 0.25$ and amplitude $S = 1$. It can be seen that the difference in the discharge obtained for the actual groove and for the same groove with its shape approximated by the leading Fourier mode from its Fourier expansion is less than 1 %. This demonstrates that the concept of the reduced geometry model can be used in the analysis of turbulent flows and thus further discussion is focused on sinusoidal grooves only. It shall be noted that although there are indications that the reduced geometry model works for turbulent flows, the assessment of uncertainties herein is approximate.

ΔQ	Original shape (%)	First Fourier mode (%)
Triangular $(a = c, b = 0)$	5.04	4.82
Trapezoidal $(a = c = b/2)$	8.75	8.43
Trapezoidal $(a = c = b/4)$	10.11	9.48

TABLE 5. Comparison of the discharge through the grooved channel with $\alpha = 0.25$ and $S = 1$ determined using the actual groove geometry as well as its approximation in the form of a leading Fourier mode from its Fourier expansion for $Re_\tau = 180$.

α	S	0	0.25	0.5	1	1.5
0.25				$Y*$	Y	
0.33				Y	Y	
0.4					$Y*$	
0.5		Y	Y	$Y*$	Y	Y
0.67				Y	Y	
1				Y	Y	
2				$Y*$	Y	

TABLE 6. List of the groove configurations studied. 'Y' identifies configurations studied using only DES and '$Y*$' identifies configurations studied using both DNS and DES.

4.4. *Analysis of flows in channels with sinusoidal grooves*

We shall now discuss the characteristics of turbulent flows in channels with sinusoidal grooves. The channel geometry is described by (3.6) and the computations have been carried out for $Re_\tau = 180$ ($Re_{2H} \approx 6000$) using $64 \times 128 \times 64$ mesh and $\Delta t = 0.002$. DNS has been used only for a few geometries (see table 6) due to high computational cost for channels with long-wavelength grooves.

Figure 8 displays variations of the difference between the discharges through the corrugated and smooth channels generated by the same pressure gradient. The existence of a critical groove wavenumber α_c, which separates the discharge-increasing grooves from the discharge-reducing grooves, is clearly documented. The critical wavenumber is estimated to be $\alpha_c \approx 1$ for $S = 0.5$ and approximately $\alpha_c \approx 0.8$ for $S = 1$. These values are similar to the α_c found in laminar flows ($\alpha_c = 1.2$). An increase of the groove amplitude S decreases the discharge when $\alpha > \alpha_c$ and, conversely, increases the discharge when $\alpha < \alpha_c$. A decrease of α increases the discharge but this increase rapidly approaches an asymptotic limit where any further decrease of α brings in negligible contributions. The highest increase of the discharge at $S = 0.5$ is approximately 2%–3%, and it is approximately 9% at $S = 1$. The maximization of the discharge requires the use of the minimum possible groove wavenumber α as well as the largest possible groove amplitude S.

Figure 9 displays distributions of U in spanwise cross-sections. The fluid either accelerates or retains its velocity in the wide segment of the channel and slows down in the narrow segment. When $\alpha < \alpha_c$ (figure 9a–d), the difference between the maximum velocity in the widest and narrowest sections of the channel is larger than the similar difference for channels with $\alpha > \alpha_c$ (figure 9e,f). The velocity maximum at the widest section of the channel for $\alpha < \alpha_c$ is higher than the maximum velocity in the smooth channel ($U \approx 19$; figure 10) and this results in an increase in the discharge. The discharge increase is most pronounced for conditions used in figure 9(b) where
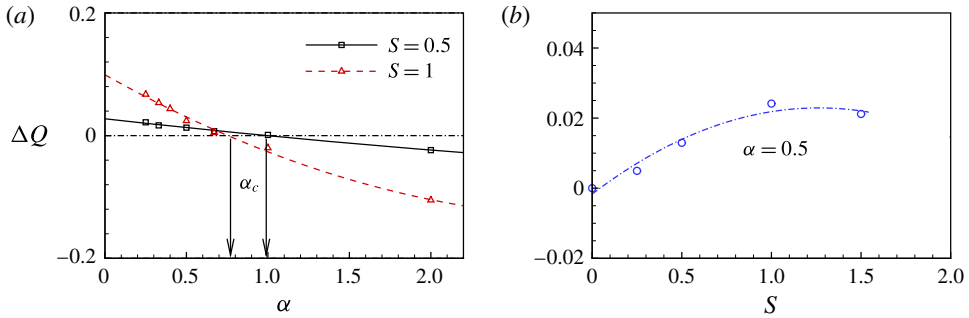
FIGURE 8. (Colour online) Variations of the discharge correction ΔQ as a function of the groove wavenumber α, (*a*) and as a function of the groove amplitude S (*b*) for channel with geometry described by (3.6) for $Re_\tau = 180$. Symbols identify computed cases while lines result from interpolation.

the maximum velocity reaches value of $U \approx 24$. When $\alpha > \alpha_c$ (figure 9*e*,*f*), the maximum velocity in the widest portion of the channel is $U \approx 18$–19, which is similar to that found in the smooth channel and, since velocity decreases in the narrow section, there is an overall reduction in the discharge.

The effect of the grooves on the flow discharge is qualitatively similar to that found in laminar flows. The presence of the grooves results in the rearrangement of the bulk motion which leads to the formation of stream tubes of high velocity fluid centred at the widest channel opening, as illustrated in figure 9. The stream tubes exist for $\alpha < \alpha_c$ as well as for $\alpha > \alpha_c$ but play a different role in each case. The difference is illustrated in figure 11 which displays distributions of U in the y–z plane. It can be seen that the flow is redirected towards the wider channel section when $\alpha < \alpha_c$ with a minor velocity decrease in the narrow section; it is the increase of the channel opening in the widest section which dominates the discharge. When $\alpha > \alpha_c$, the flow is 'choked' in the narrowest section while it retains the original velocity in the widest section; it is the decrease of the channel opening in the narrowest section which dominates the discharge.

The lack of smoothness of velocity contours in figure 9 is due to the turbulent structures whose effect has not been completely eliminated by the averaging procedure. The scale of these structures depends on the wall length scale l^* but is almost independent of the groove wavelength (compare figures 9 and 11).

We shall now discuss changes in the velocity profiles resulting from the introduction of the grooves. The velocity profile for the smooth wall consists of three layers, i.e.

(i) viscous sub-layer, ($y^+ < 7$, where $U = y^+$),
(ii) buffer layer, ($7 < y^+ < 30$) and
(iii) inertial sub-layer, ($y^+ > 30$, $U = (1/\kappa) \ln y^+ + C$, with $\kappa \approx 0.38$–0.41 and $C \approx$ 5–5.5).

The velocity profiles in the corrugated channel for conditions leading to an increase in discharge ($\alpha = 0.5$, $S = 0.5$) and a reduction in discharge ($\alpha = 2$ and $S = 0.5$) are displayed in figure 12 for three locations in the spanwise direction; plane 1 corresponds to the narrowest channel opening, plane 2 corresponds to the mean channel opening (the neutral section) and plane 3 corresponds to the widest channel opening (see figure 12*a*). In all cases, the velocity profiles consist of the linear region, the buffer region and the log-law region, similarly as in the smooth channel.
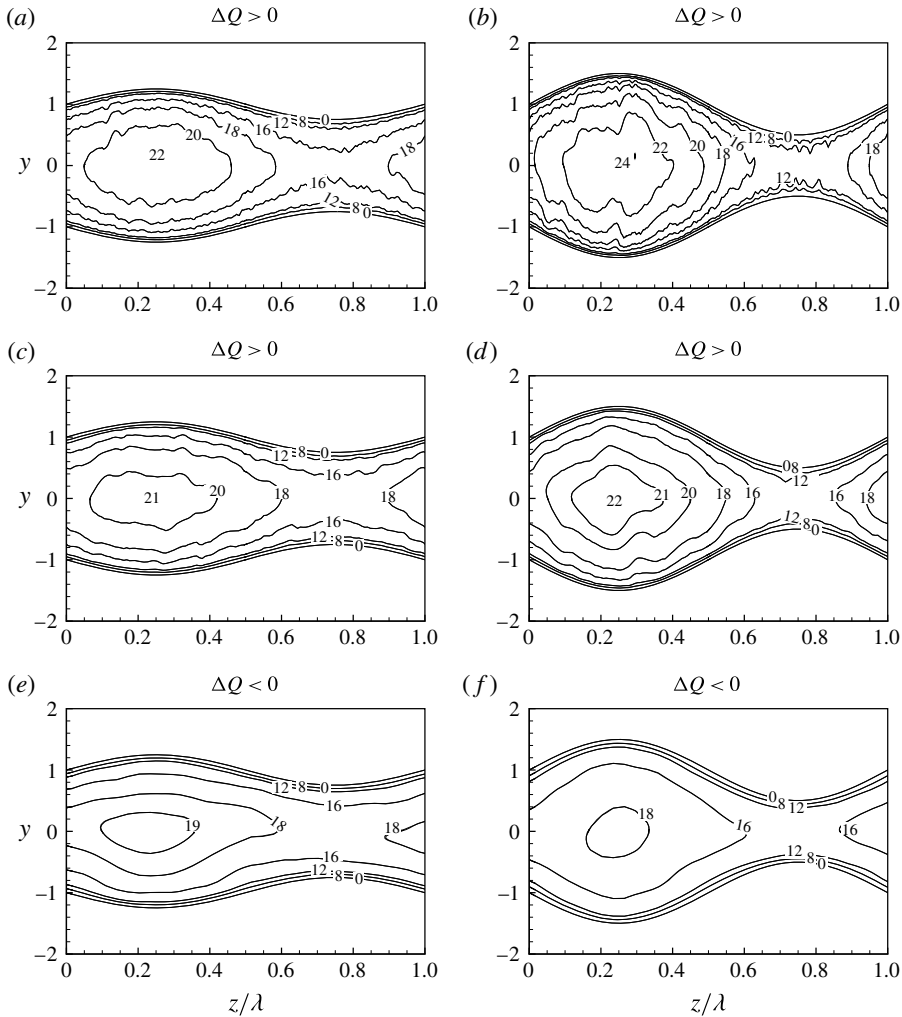
FIGURE 9. Distributions of the mean velocity component U in the y–z plane of channel with geometry described by (3.6) with $\alpha = 0.25$, $S = 0.5$ (a), $\alpha = 0.25$, $S = 1$ (b), $\alpha = 0.5$, $S = 0.5$ (c), $\alpha = 0.5$, $S = 1$ (d), $\alpha = 2$, $S = 0.5$ (e) and $\alpha = 2$, $S = 1$ (f) for $Re_\tau = 180$.

In the case of the discharge increase ($\alpha = 0.5$, $S = 0.5$), the velocity profile in plane 2 is nearly identical to the velocity in the smooth channel. The velocity in plane 1 (the narrowest opening) is smaller than in the smooth channel resulting in smaller $\partial U/\partial y^+$ at the wall (see figure 12d). The velocity in plane 3 (the widest opening) is higher than in the smooth channel with the difference increasing as y^+ increases. In the case of the discharge reduction ($\alpha = 2$, $S = 0.5$), U in plane 2 is smaller than in the smooth channel resulting in smaller $\partial U/\partial y^+$. Values of U in the remaining planes are slightly smaller than in the smooth channel for $y^+ < 20$ (see figure 12e); as y^+ increases, the velocity in plane 3 (the widest channel opening) becomes similar to that in the smooth channel while the velocity in plane 1 (the narrowest channel opening) becomes smaller than in the smooth channel.
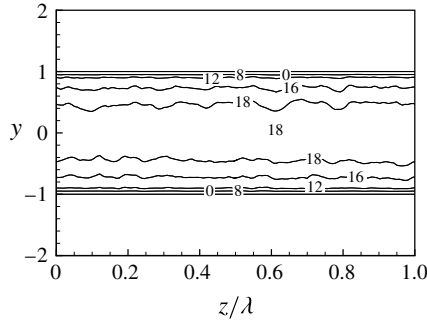
FIGURE 10. Distribution of the mean velocity component U in the y–z plane of a smooth channel and averaged only in the streamwise direction for $Re_\tau = 180$.
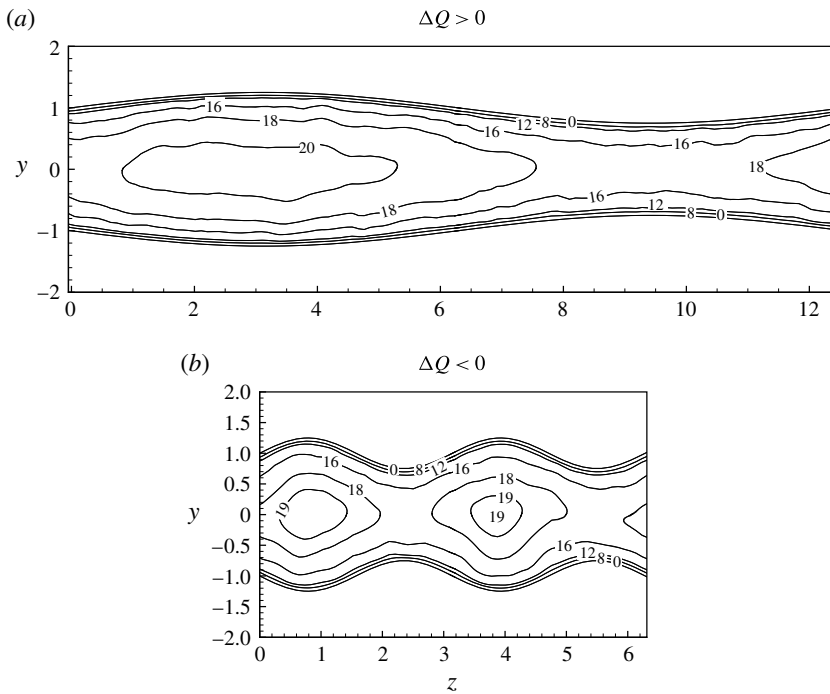

FIGURE 11. Distributions of the mean velocity U in the y–z plane for channel geometry described by (3.6) with $\alpha = 0.5$, $S = 0.5$ (*a*) and with $\alpha = 2$, $S = 0.5$ (*b*) for $Re_\tau = 180$.

4.5. *Skin friction*

An understanding of the skin friction is essential as it describes the mechanism responsible for drag creation. The total drag is unaltered by the addition of the grooves as the mean pressure gradient is kept unchanged. Thus, the integration of the shear stress over the wetted area must produce the same result regardless of the groove shape while the discharge may vary significantly depending on the groove shape. The reader may note that the addition of the grooves increases the wetted area and thus an increase in the discharge may occur only if the shear decreases sufficiently in order to balance the larger wetted area. Variations of the normalized
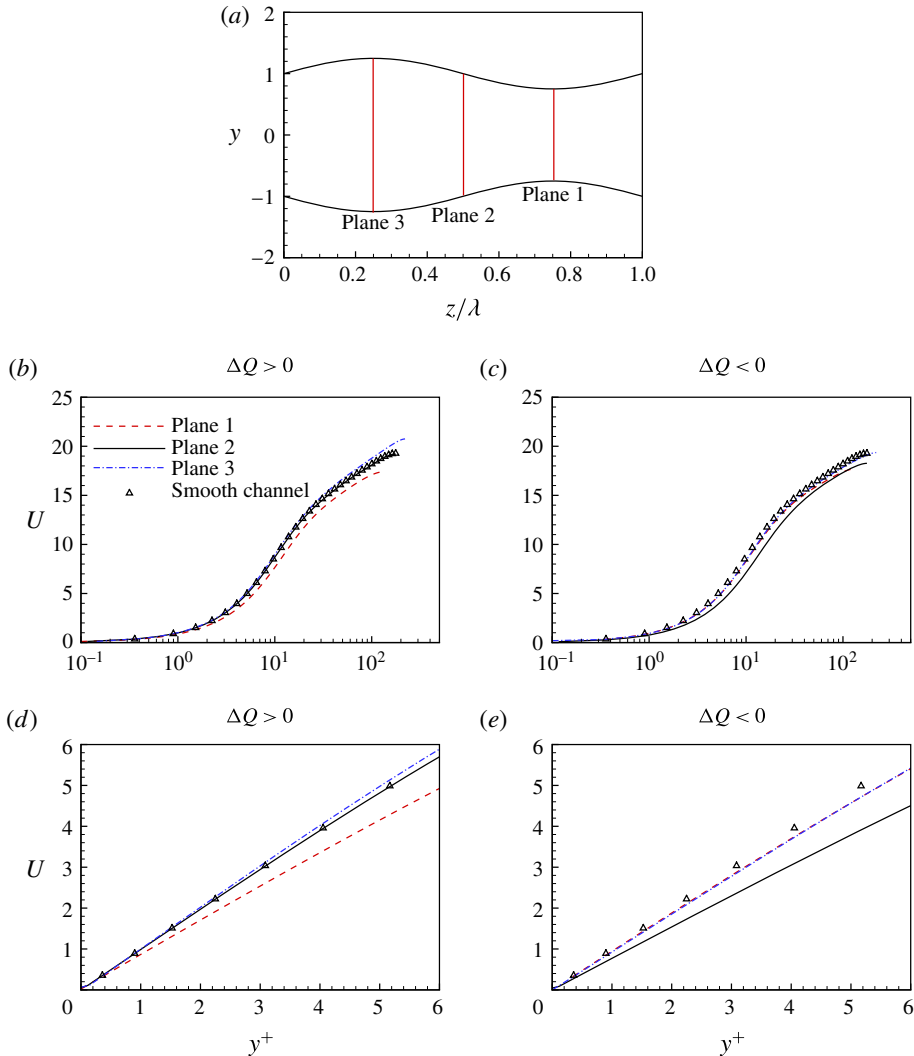
FIGURE 12. (Colour online) Variations of the mean velocity U as a function of y^+ at three spanwise locations identified in (*a*) for channel geometry described by (3.6) with $\alpha = 0.5$, $S = 0.5$ (*b,d*) and with $\alpha = 2$, $S = 0.5$ (*c,e*) for $Re_\tau = 180$. The origins of the y-coordinates at different planes have been overlapped to simplify comparisons.

skin friction Sm/Sm_0 are presented in figure 13(*b,c*). Here the projected area represents the projection of the actual surface onto the plane $y = $ const. and it is the same as the relevant area of the smooth channel.

Data displayed in figure 13(*a*) provide a comparison between the distribution of the local shear stress ($Sm(0, z)$ on a slice at $x = 0$) and its streamwise average ($Sm(z)$). Spanwise fluctuations of the local shear stress at a specific x-location are reduced when the streamwise averaging is used (see figure 13*a*). We shall use the streamwise averaged data in the following discussion.

Figure 13(*b*) depicts the effect of the groove wavenumber on the skin friction. When $\alpha < \alpha_c$ in the discharge-increase case, $Sm/Sm_0 > 1$ in the wide section and $Sm/Sm_0 < 1$
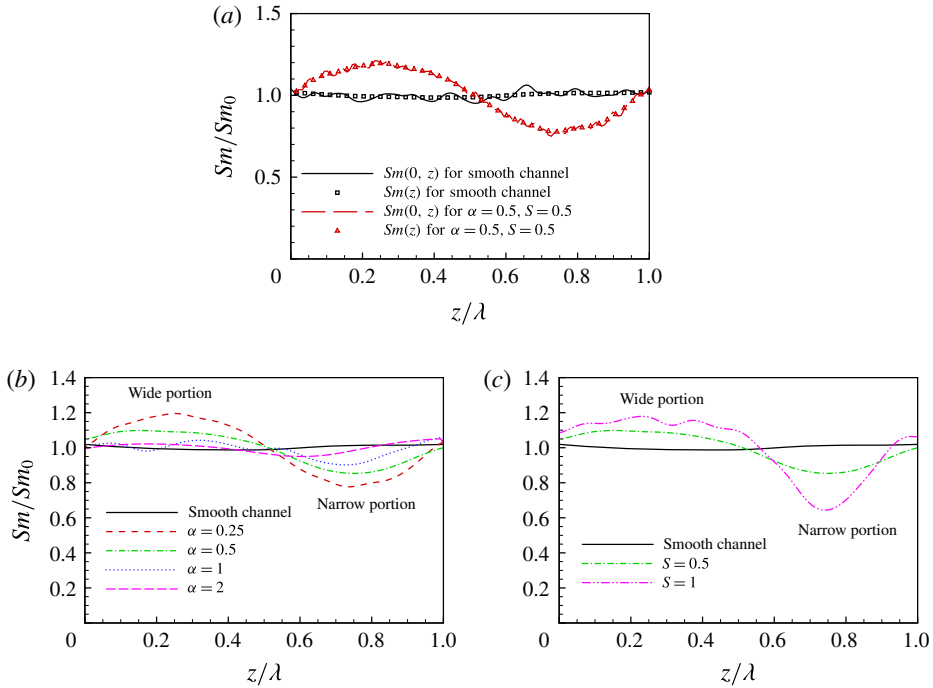
FIGURE 13. (Colour online) The normalized shear acting on the corrugated surface in a channel with geometry described by (3.6) for $Re_\tau = 180$. Comparison of the streamwise averaged and non-averaged data is given in (*a*). The spanwise distributions for $S = 0.5$ and selective α are given in (*b*), and for $\alpha = 0.5$ and selective S are given in (*c*).

in the narrow section. Reduction of α produces larger Sm/Sm_0 in the wide section and smaller Sm/Sm_0 in the narrow section (compare results for $\alpha = 0.25$ and 0.5). When $\alpha > \alpha_c$ in the discharge reduction case, $Sm/Sm_0 \approx 1$ in both the wide and narrow sections. The physical distance between these two sections are small, which results in similar momentum transport characteristics and leads to a more uniform skin friction. The reader may note that the shear variations in the streamwise direction must average out as the mean stress Sm/Sm_0 is always 1 (the total drag remains the same).

Figure 13(*c*) illustrates the effects of the groove amplitude for $\alpha = 0.5 < \alpha_c$. Sm/Sm_0 in the wide section increases with increasing S, but decreases in the narrow section. This is due to the fact that the larger groove amplitude accentuates the velocity difference between the wide and narrow sections of the channel.

4.6. *The turbulent flow quantities*

It has been documented so far that the presence of the grooves leads to the rearrangement of the mean velocity profile which results in an increase in the discharge. We shall now discuss how the turbulence characteristics change in response to the grooves.

The components of the turbulent kinetic energy (TKE) $k = (\langle u'^2 \rangle + \langle v'^2 \rangle + \langle w'^2 \rangle)/2$ and the dominant component of Reynolds shear stress ($\langle u'v' \rangle$) for grooves with $\alpha = 0.5$, $S = 0.5$ and $\alpha = 2$, $S = 0.5$, determined using DNS, are displayed in figures 14 and 15
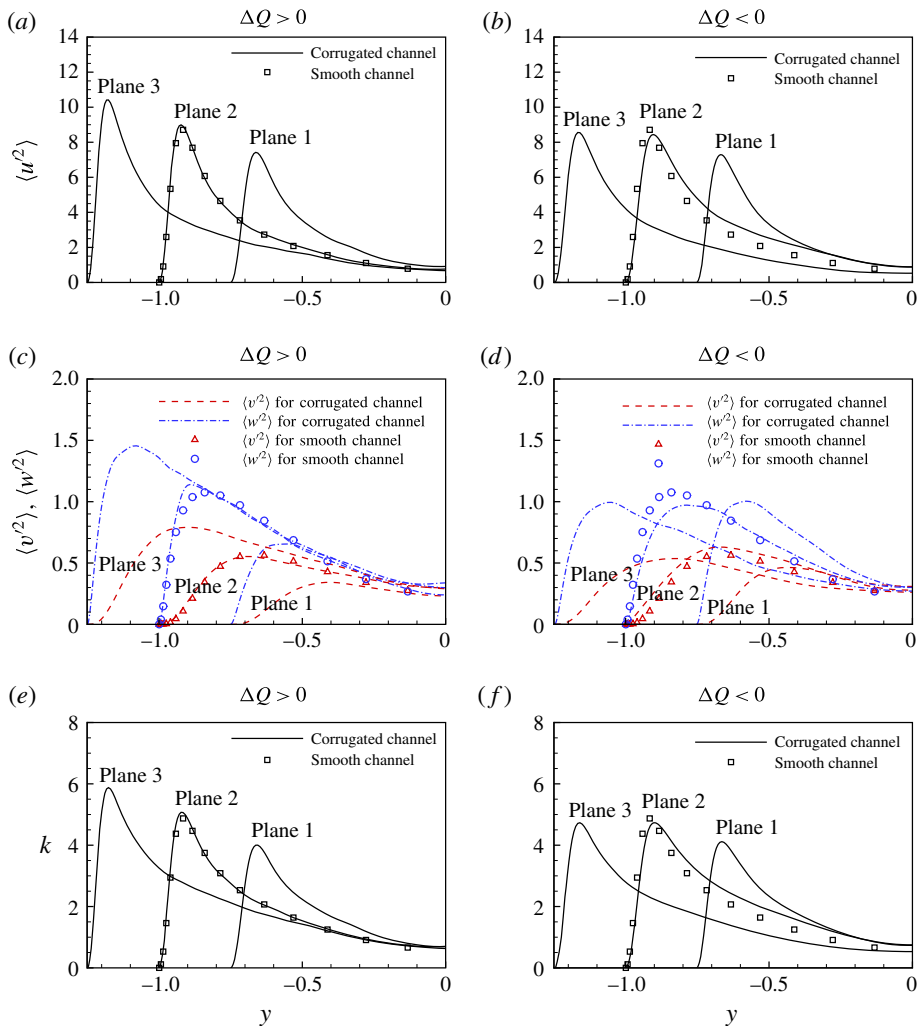
FIGURE 14. (Colour online) Distributions of the TKE in the corrugated and smooth channels for $Re_\tau = 180$. (*a*) and (*c*) display $\langle u'^2 \rangle$, $\langle v'^2 \rangle$ and $\langle w'^2 \rangle$ for grooves described by (3.6) with $\alpha = 0.5$, $S = 0.5$ while (*b*) and (*d*) display the same quantities for $\alpha = 2$, $S = 0.5$. The total kinetic energy total k is displayed in (*e*) and (*f*) for $\alpha = 0.5$, $S = 0.5$ and $\alpha = 2$, $S = 0.5$, respectively.

respectively. Our intention is to show and highlight the behaviour of the dominant component of Reynolds stress $\langle u'v' \rangle$ at the three planes in comparison to the smooth channel at plane 2. The remaining components of (lower magnitude) Reynolds stress $\langle u'w' \rangle$ and $\langle v'w' \rangle$ are plotted in the y–z plane for comparison of the different cases as shown in figure 16. It should be noted that $\langle u'w' \rangle$ and $\langle v'w' \rangle$ are zero for a smooth channel.

Figure 14 displays data for the narrowest channel opening (plane 1 in figure 12*a*), the mean opening (plane 2) and the widest opening (plane 3). Note that the y-axis used herein based on the same y origin location is different from the y^+ starting from wall used in figure 12. The qualitative characteristics of variations of all quantities in
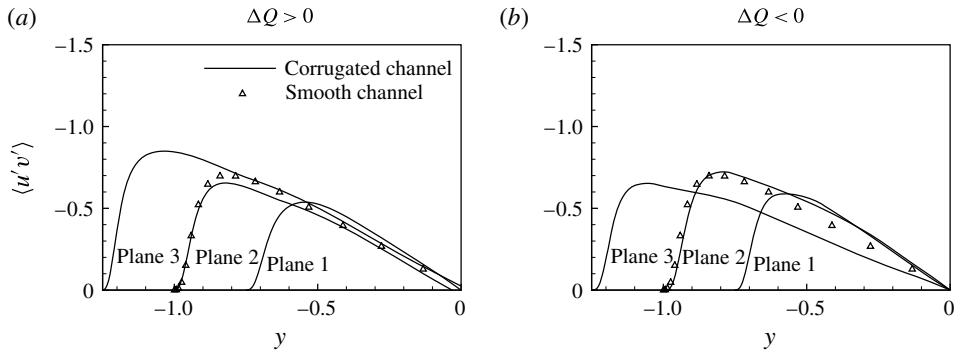
FIGURE 15. Distributions of $\langle u'v' \rangle$ in the corrugated channel with shape described by (3.6) and in the smooth channel for $Re_\tau = 180$. Data displayed in (*a*) correspond to $\alpha = 0.5$, $S = 0.5$ (discharge-increase case); data displayed in (*b*) correspond to $\alpha = 2$, $S = 0.5$ (discharge-reduction case).

all planes are similar to those found in the smooth channel, i.e. they rapidly increase in the viscous sub-layer ($y^+ < 15$), reach peak values in the buffer layer ($y^+ \approx 15$) and decrease in the inertial sub-layer ($y^+ > 15$).

Results displayed in figure 14(*a,c,e*) demonstrate that all quantities in plane 2 for $\alpha = 0.5 < \alpha_c$ (discharge-increase case) are nearly the same as in the smooth channel. The peak values in plane 1 (the narrowest section) are lower than in the smooth channel, which is possibly due to the maximum velocity being smaller than in the smooth channel. The peak values in plane 3 (the widest opening) are higher than those in the smooth channel due to the maximum velocity being larger than in the smooth channel. In the discharge-reduction case ($\alpha = 2 > \alpha_c$) the situation becomes more complex (see figure 14*b,d,f*). In plane 2 (the neutral section), $\langle u'^2 \rangle$ is slightly smaller than in the smooth channel in both the viscous sub-layer and the buffer layer, but is slightly larger in the inertial sub-layer. One may conclude that the distribution of $\langle u'^2 \rangle$ in this plane shifts towards the centre of the channel when compared to the smooth channel. In plane 1, the peak of $\langle u'^2 \rangle$ is smaller than in the smooth channel, and similar to plane 1 for the discharge-increase case ($\alpha = 0.5$). The peak of $\langle u'^2 \rangle$ in plane 3 is similar to the smooth channel and, thus, smaller than that in the discharge-increase case. Both $\langle v'^2 \rangle$ and $\langle w'^2 \rangle$ in all three planes are approximately similar to the smooth channel, which is possibly due to the weak rearrangement of the bulk motion. One can observe that $\langle u'^2 \rangle$ represents the largest component of TKE and, thus, it dictates the properties of TKE.

Figure 15 displays distributions of $\langle u'v' \rangle$. In the discharge-increase case ($\alpha = 0.5$), its magnitude in plane 2 (the neutral section) is slightly smaller than in the smooth channel, it is smaller in plane 1 (the narrowest section) and it is larger in plane 3 (the widest section). In the discharge-reduction case ($\alpha = 2$), its magnitude in plane 2 is smaller within the viscous sub-layer and in the buffer layer but slightly larger within the inertial sub-layer. In plane 1 (the narrowest section), the peak values are lower than in the smooth channel. In plane 3 (the widest section), the peak value is similar to that in plane 1.

It can be concluded that in the discharge-increase case ($\alpha < \alpha_c$), TKE and Reynolds shear stress $\langle u'v' \rangle$ in the wide section are higher and in the narrow section are smaller than in the smooth channel. In the discharge-reduction case ($\alpha > \alpha_c$), TKE
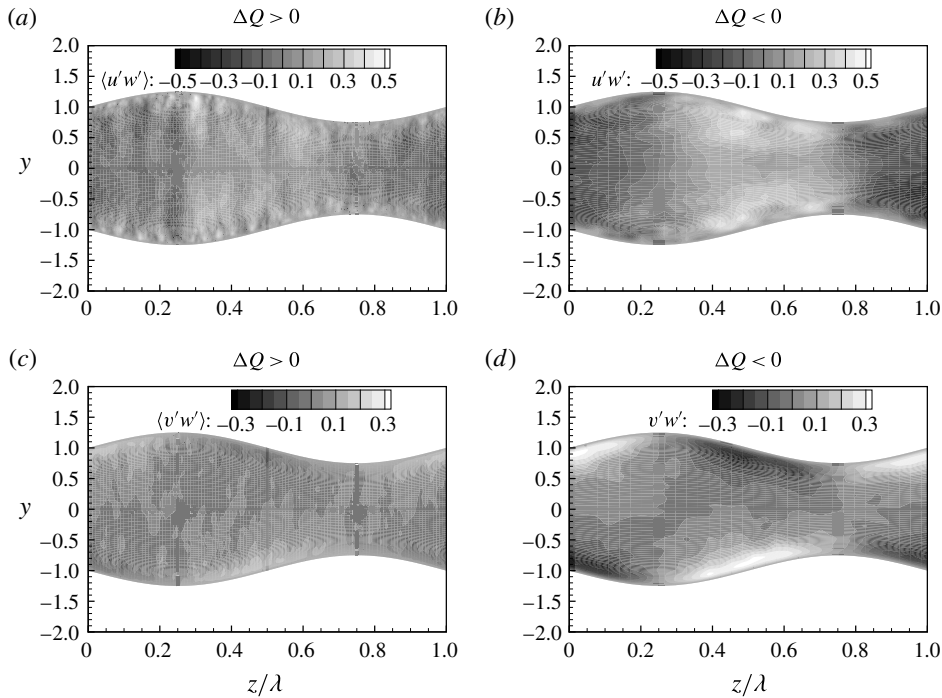
FIGURE 16. Distributions of $\langle u'w' \rangle$ and $\langle v'w' \rangle$ in the corrugated channel with shape described by (3.6) for $Re_\tau = 180$. Data displayed in (*a*) and (*c*) correspond to $\alpha = 0.5$, $S = 0.5$ (discharge-increase case); data displayed in (*b*) and (*d*) correspond to $\alpha = 2$, $S = 0.5$ (discharge-reduction case).

and Reynolds shear stress $\langle u'v' \rangle$ are smaller in the narrow section and similar to the smooth channel in the wide section. The distributions of TKE and Reynolds shear stress $\langle u'v' \rangle$ shift towards plane 2 (neutral plane) for the discharge-reduction case ($\alpha > \alpha_c$). This may be due to the smaller physical distance between the wide and narrow sections and, hence, larger spanwise velocity gradients which, in turn, produce more intense turbulent fluctuations near the neutral plane.

In order to show the complexity of distributions of Reynolds shear stresses $\langle u'w' \rangle$ and $\langle v'w' \rangle$, these quantities are presented in the form of contour plots in the *y–z* plane (see figure 16) rather than as 1-D cuts along the *y*-axis in planes 1, 2, 3 as such cuts do not exhibit any distinctive features. The theoretical arguments suggest that $\langle u'w' \rangle$ and $\langle v'w' \rangle$ should be zero in the smooth channel and very close to zero in numerical simulation of such a flow with non-zero values arising from numerical round-off errors. One may interpret $\langle u'w' \rangle$ and $\langle v'w' \rangle$ as representing the interactions between the fast fluid in the wide section of the channel and the slow fluid in the narrow section. As a result, the highest magnitudes of $\langle u'w' \rangle$ and $\langle v'w' \rangle$ are located around plane 2 (neutral plane) where the strongest spanwise interactions occur. Such interactions for the discharge-reduction case ($\alpha = 2$) are more intense than for the discharge-increase case ($\alpha = 0.5$) because of the reduction in the physical distance between the wide and narrow sections of the channel.

The effects of the groove wavenumber can be clarified by looking at the volume-averaged values of TKE [*k*] and the absolute values of the Reynolds shear stresses
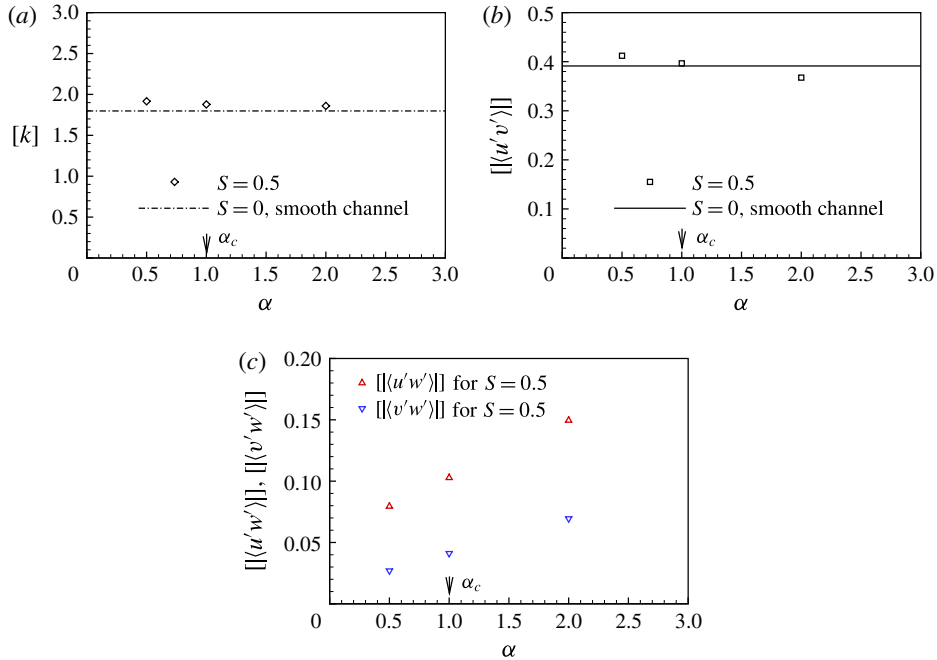
FIGURE 17. (Colour online) The volume-averaged (*a*) TKE [*k*]; (*b*) $[|\langle u'v'\rangle|]$; (*c*) $[|\langle u'w'\rangle|]$ and $[|\langle v'w'\rangle|]$ for $Re_\tau = 180$.

$[|\langle u'v'\rangle|]$, $[|\langle u'w'\rangle|]$, $[|\langle v'w'\rangle|]$, which are displayed in figure 17 for $\alpha = 0.5, 1, 2$ with $S = 0.5$. The volume-averaging operator [ ] is defined as

$$[\natural] = \frac{\displaystyle\int_\Omega \natural \, dV}{\displaystyle\int_\Omega dV}. \qquad (4.7)$$

The reader may note that $[|\langle u'w'\rangle|]$ and $[|\langle v'w'\rangle|]$ are both zero in the smooth channel. The volume-averaged TKE [*k*] for the corrugated channel is slightly higher (approximately 6 %) than that for the smooth channel, $[|\langle u'w'\rangle|]$ and $[|\langle v'w'\rangle|]$ are also higher than in the smooth channel and increase with increasing wavenumber. $[|\langle u'v'\rangle|]$ in the corrugated channel is slightly higher than in the smooth channel for the discharge increase case ($\alpha = 0.5$) and is slightly lower for the discharge reduction case ($\alpha = 2$).

The above discussion shows that corrugations can rearrange the distribution of TKE and the Reynolds stress, but are unable to significantly reduce the global turbulence intensity.

The distributions of the TKE and the Reynolds stress discussed in the previous section imply that there is less turbulent activity in the narrow portion of the corrugated channel and stronger turbulent activity in the wide portion in the discharge-increase case ($\alpha < \alpha_c$). We shall now look at the turbulence structures in order to better understand the character of the flow in each case.

In figure 18, the ensemble time-averaging Reynolds shear stress $\langle u'v'\rangle$ is presented with quadrant detection for ejection events (Q2) and for sweep events (Q4).
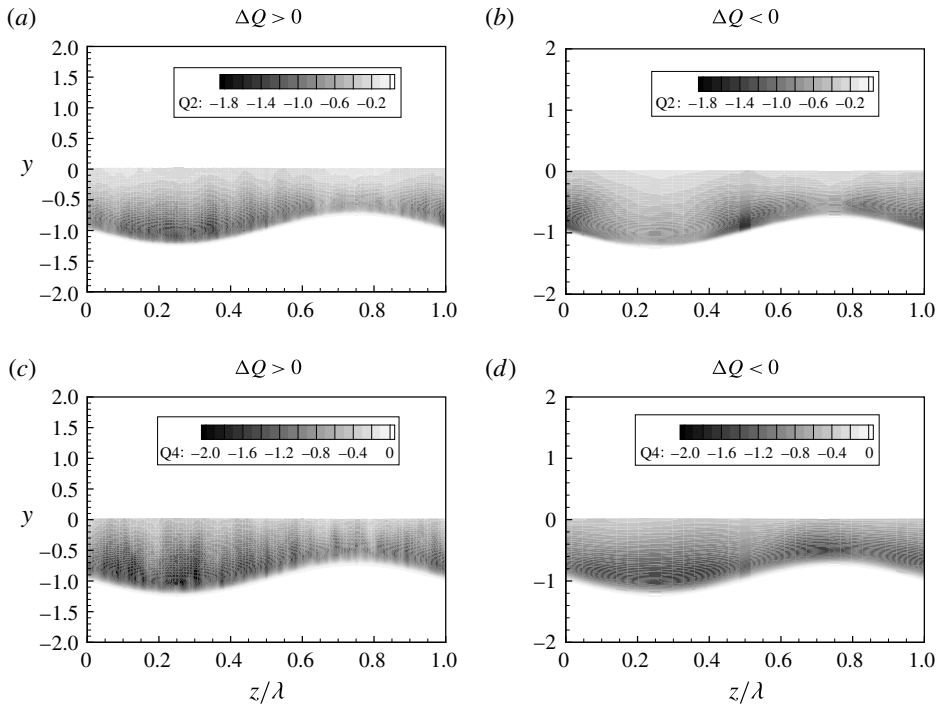
FIGURE 18. Ensemble time-averaging Reynolds shear stress $\langle u'v' \rangle$ with quadrant detection (Q2 for ejection events (*a,b*) and Q4 for sweep events (*c,d*)) in a corrugated channel described by (3.6) with $\alpha = 0.5$, $S = 0.5$ (*a,c*) and with $\alpha = 2$, $S = 0.5$ (*b,d*) for $Re_\tau = 180$.

Figure 18(*a,c*) demonstrates that in the discharge increase case ($\alpha < \alpha_c$) most of the near-wall turbulent motions (ejection and sweep) tend to gather in the wide section of the channel. This may be due to the fact that the maximum velocity in the wide portion is much larger than that in the narrow portion. An increase in the ejection/sweep suggests the occurrence of more intense bursting phenomena, stronger turbulent motions and higher TKE, and this is consistent with the findings presented in figures 14(*a,e*) and 15(*a*).

Results presented in figure 18(*b*) demonstrate that in the discharge-reduction case ($\alpha > \alpha_c$) the ejection motions tend to occur in the neutral section, which may be associated with the strong velocity gradient between the wide and narrow sections with a short physical distance between them. Figure 18(*d*) shows that there is no obvious tendency of gathering of sweep motions either in the wide or in the narrow portions of the channel, which is balanced by the momentum transport between the wide and narrow sections. This observation is consistent with the results displayed in figures 14(*b,f*) and 15(*b*). It is very interesting to observe that the ejection and sweep behave differently in the discharge-increase and discharge-reduction cases.

In summary, the analysis of TKE, the Reynolds stress and the turbulent structures shows that the turbulence intensity in the narrow portion of the channel is suppressed. When the groove amplitude is high ($S \to 2$), the narrow section shrinks to a triangular corner and the flow is expected to relaminarize (Eckert & Irvine Jr 1956). These results led to the creation of the concept of riblets for turbulent drag reduction (Walsh & Weinstein 1978; Walsh & Lindeman 1984).

4.7. *Analysis of flow changes caused by the small-wavenumber grooves*

Interactions between the wide and narrow sections of the channel weaken when $\alpha \to 0$ and thus each section might behave as a smooth channel but with different heights and the same pressure gradient.

First, we shall demonstrate that the local flow properties become very similar when expressed in terms of the local scales. The local half-channel height δ^*, the local friction velocity $u_{\tau e}^*$, the local friction Reynolds number $Re_{\tau e}$ and the local wall length l_e^* are defined as

$$\delta^* = H^* \left(1 + \frac{S}{2} \sin \alpha z \right), \tag{4.8a}$$

$$u_{\tau e}^* = \sqrt{\frac{\beta^* \delta^*}{\rho^*}}, \tag{4.8b}$$

$$Re_{\tau e} = \frac{u_{\tau e}^* \delta^*}{\nu^*} = Re_\tau \left(1 + \frac{S}{2} \sin \alpha z \right)^{3/2}, \tag{4.8c}$$

$$l_e^* = \frac{\nu^*}{u_{\tau e}^*}, \tag{4.8d}$$

where the subscript $_e$ stands for local scalar and the superscript * stands for dimensional scalar.

It can be shown that the ratio between the local and the average friction velocities, the average streamwise velocity scaled with the local friction velocity denoted as U_e and the wall distance scaled with the local wall length denoted as y_e^+ are of the form

$$\frac{u_{\tau e}^*}{u_\tau^*} = \left(1 + \frac{S}{2} \sin \alpha z \right)^{1/2}, \tag{4.9a}$$

$$U_e = \frac{U^*}{u_{\tau e}^*} = \frac{U}{\left(1 + \dfrac{S}{2} \sin \alpha z \right)^{1/2}}, \tag{4.9b}$$

$$y_e^+ = \frac{y^*}{\nu^*/u_{\tau e}^*} = y^+ \left(1 + \frac{S}{2} \sin \alpha z \right)^{1/2}. \tag{4.9c}$$

Distributions of U and U_e as functions of y^+ and y_e^+ are presented in figure 19(a,b), respectively. The velocity distributions in the widest, mean and narrowest sections of the corrugated channel are similar to the smooth channel when the local scales are used (figure 19b) but different when the original scales are used (figure 19a). Distributions of the largest component of TKE, $\langle u'^2 \rangle$, displayed in figure 20 demonstrate that the values for all three planes nearly overlap when scaled using the local scales. This suggests that properties of the flow in different planes can be deduced from properties of the flow in a smooth channel through the use of the proper scaling.

Use of (4.3), (4.9b) and (4.9c) leads to the local velocity gradient at the wall of the form

$$\frac{\partial U}{\partial y} = \frac{\partial U_e}{\partial y_e^+} Re_\tau \left(1 + \frac{S}{2} \sin \alpha z \right). \tag{4.10}$$
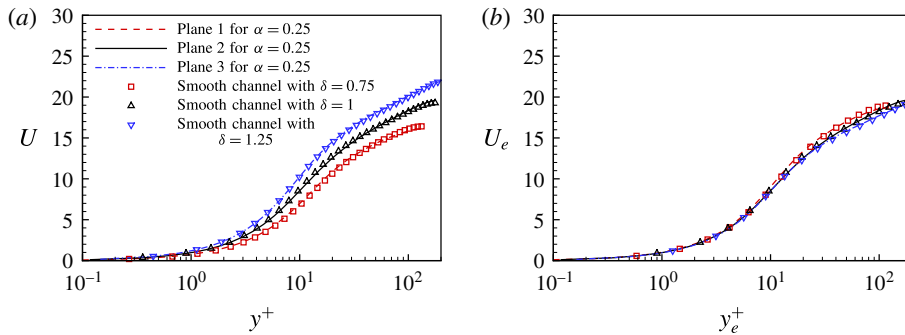
FIGURE 19. (Colour online) Distributions of the average mean velocity U for $Re_\tau = 180$ as a function of y^+ (a) and the local mean velocity U_e as a function of y_e^+ (b) at the widest, mean and narrowest sections of channel with geometry described by (3.6) with $\alpha = 0.25$ and $S = 0.5$. Symbols identify velocities in the smooth channels with different mean openings.
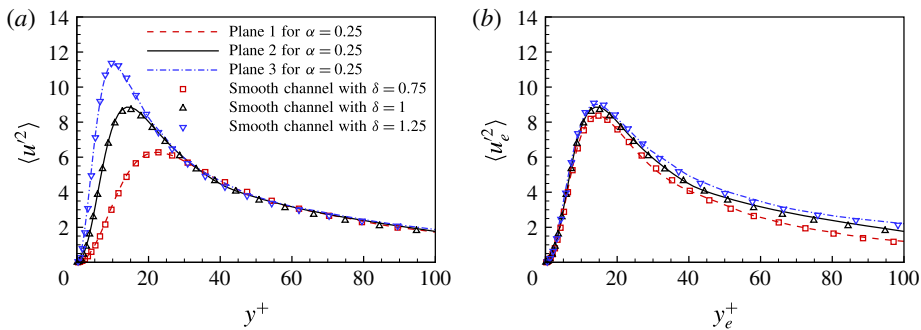

FIGURE 20. (Colour online) Distributions of $\langle u'^2 \rangle$ as functions of y^+ (a) and $\langle u_e'^2 \rangle$ as functions of y_e^+ (b) for $Re_\tau = 180$ at the widest, mean and narrowest sections of channel with geometry described by (3.6) with $\alpha = 0.25$ and $S = 0.5$. Symbols identify velocities in the smooth channels with different mean openings.

As $\partial U_e / \partial y_e^+ = 1$ near the wall,

$$\frac{Sm}{Sm_0} = 1 + \frac{S}{2} \sin \alpha z. \qquad (4.11)$$

Figure 21 displays the distribution of Sm/Sm_0 given by (4.11) together with DNS results. When α decreases, Sm/Sm_0 approaches the theoretical estimate. Values computed for $\alpha = 0.25$ are already very close to the theoretical estimate, implying that the interactions between fluid flowing in different sections of the corrugated channel at $\alpha = 0.25$ are very weak and could be neglected.

The above discussion shows that the velocity distribution in an arbitrary x–y plane of the corrugated channel is similar to the smooth channel when described using the local friction velocity, the local wall length and local friction Reynolds number. Thus, the local mean velocity scaled using the local effective friction velocity $u_{\tau e}^*$ can be written as (Pope 2000)

$$U_{be} = \frac{U_b^*}{u_{\tau e}^*} = 5.6818 \log_{10} Re_{\tau e} + 3.5418, \qquad (4.12)$$
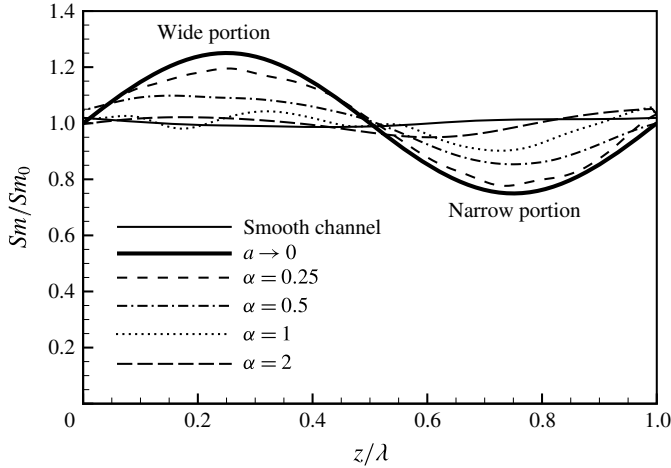
FIGURE 21. Distribution of the ratio of wall shear Sm/Sm_0 for $S = 0.5$ and $Re_\tau = 180$.

where U_b^* is the dimensional local bulk velocity, and depends on the local effective friction Reynolds number $Re_{\tau e}$. The local mean velocity scaled using the friction velocity u_τ^* can be written as

$$U_b = \left[5.6818 \log_{10} Re_\tau + 8.5227 \log_{10}\left(1 + \frac{S}{2}\sin\alpha z\right) + 3.5418\right]\left(1 + \frac{S}{2}\sin\alpha z\right)^{1/2}. \tag{4.13}$$

Integration of the mean velocity in the spanwise direction z leads to the discharge

$$Q|_{\alpha\to 0} = \frac{1}{2\pi/\alpha}\int_0^{2\pi/\alpha} 2\delta U_b \,\mathrm{d}z$$

$$= \frac{(5.6818 \log_{10} Re_\tau + 3.5418)}{\pi}\int_0^{2\pi}\left[1 + \frac{8.5227 \log_{10}\left(1 + \dfrac{S}{2}\sin\xi\right)}{[5.6818 \log_{10} Re_\tau + 3.5418]}\right]$$

$$\times \left(1 + \frac{S}{2}\sin\xi\right)^{3/2}\mathrm{d}\xi, \tag{4.14}$$

where 2δ is the local channel opening at the location z.

The discharge for a smooth channel has the form

$$Q_0|_{\alpha\to 0} = Q|_{\alpha\to 0}|_{S=0} = 2(5.6818 \log_{10} Re_\tau + 3.5418). \tag{4.15}$$

The ratio of discharges in the corrugated and smooth channels at the same friction Reynolds number (i.e. the same pressure gradient) is

$$\left.\frac{Q}{Q_0}\right|_{\alpha\to 0} = \frac{1}{2\pi}\int_0^{2\pi}\left[1 + \frac{8.5227 \log_{10}\left(1 + \dfrac{S}{2}\sin\xi\right)}{[5.6818 \log_{10} Re_\tau + 3.5418]}\right]\left(1 + \frac{S}{2}\sin\xi\right)^{3/2}\mathrm{d}\xi, \tag{4.16}$$

and gives the discharge difference of the form

$$\Delta Q|_{\alpha \to 0}(S) = \frac{Q}{Q_0}\bigg|_{\alpha \to 0} - 1. \tag{4.17}$$

The above predictions are compared with the DNS results for a channel with $S = 0.5$ and $S = 1$ at $Re_\tau = 180$. Equation (4.17) gives $\Delta Q|_{\alpha \to 0} = 1.88\,\%$ and $\Delta Q|_{\alpha \to 0} = 7.57\,\%$, respectively, while the numerical results displayed in figure 8(a) give $2\,\%$ and $10\,\%$, respectively. This suggests that the above estimate provides quite a good approximation of the discharge through the corrugated channel when the corrugation wave number is sufficiently small.

The above analysis can be extended to flow conditions not accessible to numerical simulations. As an example, consider the limit of very high friction Reynolds number. The discharge ratio for the corrugated and smooth channels is of the form

$$\lim_{Re_\tau \to \infty} \Delta Q|_{\alpha \to 0} = \frac{1}{2\pi} \int_0^{2\pi} \left(1 + \frac{S}{2}\sin\xi\right)^{3/2} \mathrm{d}\xi - 1. \tag{4.18}$$

Figure 22 displays predictions of ΔQ based on (4.17) for different Reynolds numbers and groove amplitudes for small α. Data for the laminar flow have been added for comparison. The discharge increases with S at any Re_τ. There is a significant drop in the discharge increase when the flow changes from the laminar to turbulent form. In the turbulent state, the magnitude of the discharge increase decreases very slowly as Re_τ increases but remains large enough to be of practical interest.

It has been shown in §3 that the discharge increases linearly with Re_τ in the case of laminar flow. The above analysis suggests that in the case of turbulent flows the discharge increase is nearly independent of Re_τ. The discharge increase is $7.57\,\%$ for $Re_\tau = 180$ and would be $7.28\,\%$ and $7.15\,\%$ for $Re_\tau = 395$ and 590 which are the other values of Re_τ frequently used in DNS studies. These cases have not been attempted during the present study due to computational cost and, thus, the Re_τ dependence conjectured above remains to be proven.

It can be concluded that the maximization of the discharge is achieved using grooves with decreasing wavenumber and increasing amplitude. The resulting discharge can increase $20\,\%$–$30\,\%$ above the smooth channel discharge, depending on the Reynolds number. Though this increase is not as high as in laminar flows ($150\,\%$), it is still much higher than what can be achieved using other more traditional drag-reducing methods. It can also be concluded that the discharge-increase results from the bulk velocity rearrangement rather than from the suppression of the turbulence intensity.

4.8. *Additional cases with phase shift*

The above discussion dealt with the positioning of the grooves at the upper and lower walls in such a manner that the maximum height of the upper grooves was located above the minimum height of the lower grooves, i.e. the diverging–converging configuration. It is of interest to check how the relative positioning of the upper and lower groove systems affects the flow discharge. This positioning is parameterized using the phase shift φ, i.e. the channel geometry is described as

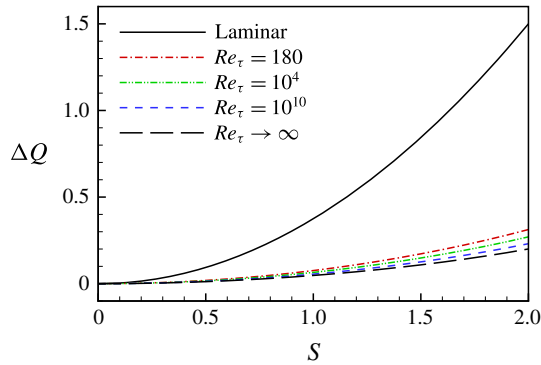$$y_L = -1 - \frac{S}{2}\sin(\alpha z), \quad y_U = 1 + \frac{S}{2}\sin(\alpha z + \varphi). \tag{4.19a,b}$$

FIGURE 22. (Colour online) Variations of the discharge correction ΔQ as a function of S at different Re_τ for $\alpha \to 0$.

Use of $\varphi = 0$ produces the converging–diverging channel and $\varphi = \pi$ results in the sinusoidal channel for $\alpha = 0.5$ and $S = 1$ (see figure 23). Results displayed in figure 24 demonstrate the converging–diverging channel produces the largest discharge increase. Increase of φ from 0 to π reduces this increase and can reduce the total discharge below the smooth channel level if φ is close enough to π. The deterioration of the system performance is associated with the reduction and eventual elimination of the stream tube with the fast moving fluid forming in the wide section of the channel, as documented in figure 23. The corresponding changes of the skin-friction distribution are documented in figure 25.

5. Concluding remarks

An analysis of the laminar and turbulent flows through corrugated channels, with the grooves being parallel to the flow direction, has been carried out. The analysis relied on the theoretical solution in the laminar case and on the DES method in the turbulent case. It has been demonstrated that the use of the grooves results in an increase of the discharge through the grooved channel when compared with a smooth channel operating under the same pressure gradient. It has been shown that the reduced geometry model applies to turbulent flows, i.e. the groove shape can be replaced by the leading Fourier mode from its Fourier representation and the resulting error is acceptable for most applications. It is therefore possible to parameterize the groove effects using just two parameters, i.e. the groove wavenumber and the groove amplitude. Detailed results have been presented for sinusoidal grooves in the range the Reynolds numbers of interest. Changes in the discharge, the mean velocity distribution, the mean shear distribution, the TKE, the Reynolds stress and the turbulence structures have been documented and discussed.

It has been shown that the corrugated channel, subject to the same pressure gradient as the smooth channel, can produce either larger or smaller discharge depending on the groove wavenumber. There exists a critical groove wavenumber $\alpha_c \approx 0.8$–1 separating both types of grooves, with grooves with $\alpha < \alpha_c$ increasing discharge. An increase of the groove amplitude S increases the discharge for $\alpha < \alpha_c$ and decreases the discharge for $\alpha > \alpha_c$. The grooves are less effective in increasing the discharge
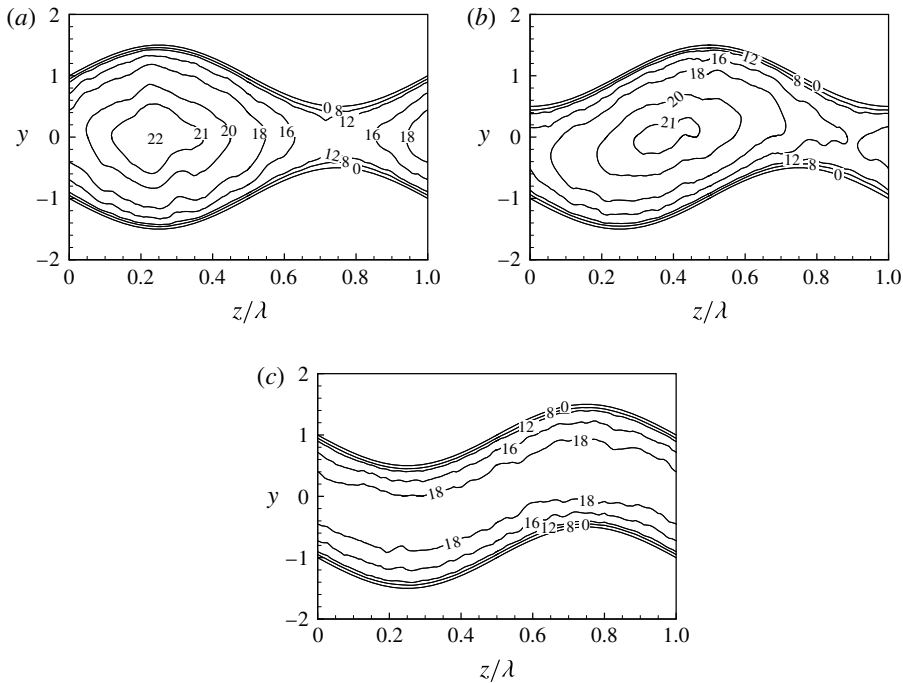
(a)

(b)

(c)

FIGURE 23. Distributions of the streamwise velocity U in the y–z plane at $Re_\tau = 180$ for $\alpha = 0.5$ and $S = 1$ with different phase shifts. (a) $\varphi = 0$; (b) $\varphi = \pi/2$; (c) $\varphi = \pi$.
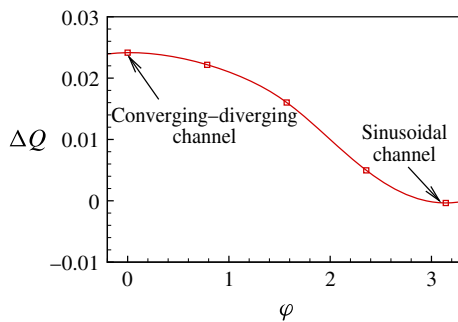
FIGURE 24. (Colour online) Variations of the discharge correction ΔQ as a function of the phase shift φ for $Re_\tau = 180$.

in turbulent flows when compared with the laminar flows. The discharge increase in the turbulent flow is approximately 10 % when $\alpha = 0.25$ and $S = 1$, which is similar to the discharge increase that can be achieved using riblets (7 %–10 %). A maximum discharge can be achieved for $\alpha \to 0$ and $S \to 2$.

The discharge increase is achieved by rearranging the bulk velocity distribution in the transverse (y–z) plane with the largest fluid flux flowing through the widest channel opening. The grooves do not suppress the TKE production and the Reynolds stress. Change of the phase shift between the groove systems at the upper and lower walls affect the bulk flow. The largest discharge increase is achieved for the
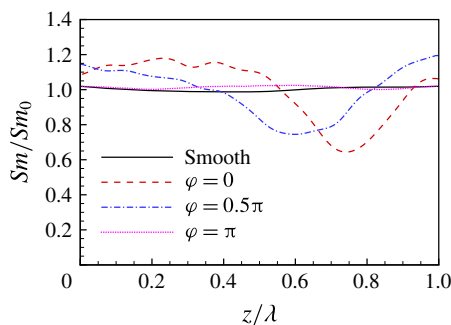
FIGURE 25. (Colour online) Distributions of the shear stress in the *y–z* plane for $\alpha = 0.5$ and $S = 1$ with different phase shifts φ at $Re_\tau = 180$.

converging–diverging form of the channel while no discharge increase can be achieved for the wavy form of the channel.

REFERENCES

ABE, H., KAWAMURA, H. & MATSUO, Y. 2001 Direct numerical simulation of a fully developed turbulent channel flow with respect to the Reynolds number dependence. *Trans. ASME J. Fluids Engng* **123** (2), 382–393.

ALEKSEEV, V. V., GACHECHILADZE, I. A., KIKNADZE, G. I. & OLEINIKOV, V. G. 1998 Tornado-like energy transfer on three-dimensional concavities of reliefs-structure of self-organizing flow, their visualisation, and surface streamlining mechanisms. In *Transactions of the 2nd Russian Nat. Conf. of Heat Transfer, Heat Transfer Intensification Radiation and Complex Heat Transfer*, vol. 6, pp. 33–42. Publishing House of Moscow Energy Institute (MEI).

BALAKUMAR, P. & WIDNALL, S. E. 1986 Application of unsteady aerodynamics to large-eddy breakup devices in a turbulent flow. *Phys. Fluids* **29** (6), 1779–1787.

BARTHLOTT, W. & NEINHUIS, C. 1997 Purity of the sacred lotus, or escape from contamination in biological surfaces. *Planta* **202** (1), 1–8.

BECHERT, D. W. & BARTENWERFER, M. 1989 The viscous flow on surfaces with longitudinal ribs. *J. Fluid Mech.* **206**, 105–129.

BECHERT, D. W., BRUSE, M. & HAGE, W. 2000 Experiments with three-dimensional riblets as an idealized model of shark skin. *Exp. Fluids* **28** (5), 403–412.

BECHERT, D. W., BRUSE, M., HAGE, W., VAN DER HOEVEN, J. G. T. & HOPPE, G. 1997 Experiments on drag-reducing surfaces and their optimization with an adjustable geometry. *J. Fluid Mech.* **338** (5), 59–87.

BURGESS, N. K., OLIVEIRA, M. M. & LIGRANI, P. M. 2003 Nusselt number behavior on deep dimpled surfaces within a channel. *Trans. ASME J. Heat Transfer* **125**, 11.

CABAL, A., SZUMBARSKI, J. & FLORYAN, J. M. 2001 Numerical simulation of flows over corrugated walls. *Comput. Fluids* **30** (6), 753–776.

CHANG, M. J., CHOW, L. C. & CHANG, W. S. 1991 Improved alternating-direction implicit method for solving transient three-dimensional heat diffusion problems. *Numer. Heat Transfer* B **19** (1), 69–84.

CHEN, Y., CHEW, Y. T. & KHOO, B. C. 2010 Turbulent flow manipulation by passive devices. In *Proceedings of the 13th Asian Congress of Fluid Mechanics*, pp. 613–616. The Asian Fluid Mechanics Committee (AFMC).

CHOI, H., MOIN, P. & KIM, J. 1993 Direct numerical simulation of turbulent flow over riblets. *J. Fluid Mech.* **255**, 503–539.

CHOI, K.-S. 1989 Near-wall structure of a turbulent boundary layer with riblets. *J. Fluid Mech.* **208**, 417–458.

CHOI, K.-S., JUKES, T. & WHALLEY, R. 2011 Turbulent boundary-layer control with plasma actuators. *Phil. Trans. R. Soc. Lond.* A **369** (1940), 1443–1458.

DANIELLO, R. J., WATERHOUSE, N. E. & ROTHSTEIN, J. P. 2009 Drag reduction in turbulent flows over superhydrophobic surfaces. *Phys. Fluids* **21** (8), 085103.

DARCY, H. 1857 *Recherches Expérimentales Relatives au Mouvement de l'Eau dans les Tuyaux.* Mallet-Bachelier.

DEAN, B. & BHUSHAN, B. 2010 Shark-skin surfaces for fluid-drag reduction in turbulent flow: a review. *Phil. Trans. R. Soc. Lond.* A **368** (1929), 4775–4806.

DOUGLAS, J. 1955 On the numerical integration of $\partial^2 u/\partial x^2 + \partial^2 u/\partial y^2 = \partial u/\partial t$ by implicit methods. *J. Soc. Ind. Appl. Maths* **3** (1), 42–45.

ECKERT, E. R. G. & IRVINE, T. F. JR. 1956 Flow in corners of passages with noncircular cross sections. *Trans. ASME* **78** (4), 709.

GAO, L. C. & MCCARTHY, T. J. 2006 A perfectly hydrophobic surface ($\theta a/\theta r = 180/180$). *J. Am. Chem. Soc.* **128** (28), 9052–9053.

GARCÍA-MAYORAL, R. & JIMÉNEZ, J. 2011 Drag reduction by riblets. *Phil. Trans. R. Soc. Lond.* A **369** (1940), 1412–1427.

GRAHAM, J. M. R. 1998 The effect of a two-dimensional cascade of thin streamwise plates on homogeneous turbulence. *J. Fluid Mech.* **356**, 125–147.

HAGEN, G. 1854 Uber den einfluss der temperatur auf die bewegung des wasser in röhren. *Math. Abh. Akad. Wiss.* **17**.

HOEPFFNER, J. & FUKAGATA, K. 2009 Pumping or drag reduction? *J. Fluid Mech.* **635**, 171–187.

INCROPERA, F. P. & DEWITT, D. P. 2002 *Fundamentals of Heat and Mass Transfer*, 5th edn. Wiley.

ITOH, M., TAMANO, S., IGUCHI, R., YOKOTA, K., AKINO, N., HINO, R. & KUBO, S. 2006 Turbulent drag reduction by the seal fur surface. *Phys. Fluids* **18**, 065102.

IUSO, G., ONORATO, M., SPAZZINI, P. G. & DI CICCA, G. M. 2002 Wall turbulence manipulation by large-scale streamwise vortices. *J. Fluid Mech.* **473**, 23–58.

JOSEPH, P., COTTIN-BIZONNE, C., BENOIT, J.-M., YBERT, C., JOURNET, C., TABELING, P. & BOCQUET, L. 2006 Slippage of water past superhydrophobic carbon nanotube forests in microchannels. *Phys. Rev. Lett.* **97** (15), 156104.

KEATING, A. & PIOMELLI, U. 2006 A dynamic stochastic forcing method as a wall-layer model for large-eddy simulation. *J. Turbul.* **7**, N12.

KIM, J. 2011 Physics and control of wall turbulence for drag reduction. *Phil. Trans. R. Soc. Lond.* A **369** (1940), 1396–1411.

KIM, J., MOIN, P. & MOSER, R. 1987 Turbulence statistics in fully developed channel flow at low Reynolds number. *J. Fluid Mech.* **177**, 133–166.

LIENHART, H., BREUER, M. & KÖKSOY, C. 2008 Drag reduction by dimples?-a complementary experimental/numerical investigation. *Intl J. Heat Fluid Flow* **29** (3), 783–791.

MARTELL, M., PEROT, J. B. & ROTHSTEIN, J. P. 2009 Direct numerical simulations of turbulent flows over superhydrophobic surfaces. *J. Fluid Mech.* **620**, 31–41.

MIN, T., KANG, S. M., SPEYER, J. L. & KIM, J. 2006 Sustained sub-laminar drag in a fully developed channel flow. *J. Fluid Mech.* **558**, 309–318.

MOHAMMADI, A. & FLORYAN, J. M. 2015 Numerical analysis of laminar-drag-reducing grooves. *Trans. ASME J. Fluids Engng* **137** (4), 041201.

MOHAMMADI, M. & FLORYAN, J. M. 2013a Groove optimization for drag reduction. *Phys. Fluids* **25** (11), 113601.

MOHAMMADI, M. & FLORYAN, J. M. 2013b Pressure losses in grooved channels. *J. Fluid Mech.* **725**, 23–54.

MOIN, P. & KIM, J. 1982 Numerical investigation of turbulent channel flow. *J. Fluid Mech.* **118**, 341–377.

MOODY, L. F. 1944 Friction factors for pipe flow. *Trans. ASME* **66** (8), 671–684.

MORADI, H. V. & FLORYAN, J. M. 2013 Flows in annuli with longitudinal grooves. *J. Fluid Mech.* **716**, 280–315.

MOSER, R. D., KIM, J. & MANSOUR, N. N. 1999 Direct numerical simulation of turbulent channel flow up to $Re_\tau = 590$. *Phys. Fluids* **11**, 943.

NIKURADSE, J. 1933 Strömungsgesetze in rauhen rohren. VDI-Forschungscheft 361; also NACA TM 1292 (1950).

OU, J., PEROT, B. & ROTHSTEIN, J. P. 2004 Laminar drag reduction in microchannels using ultrahydrophobic surfaces. *Phys. Fluids* **16** (12), 4635–4643.

OU, J. & ROTHSTEIN, J. P. 2005 Direct velocity measurements of the flow past drag-reducing ultrahydrophobic surfaces. *Phys. Fluids* **17** (10), 103606.

PARK, H. W., PARK, H. M. & KIM, J. 2013 A numerical study of the effects of superhydrophobic surface on skin-friction drag in turbulent channel flow. *Phys. Fluids* **25** (11), 110815.

POPE, S. B. 2000 *Turbulent Flows*. Cambridge University Press.

QUADRIO, M. 2011 Drag reduction in turbulent boundary layers by in-plane wall motion. *Phil. Trans. R. Soc. Lond.* A **369** (1940), 1428–1442.

QUADRIO, M., FLORYAN, J. M. & LUCHINI, P. 2007 Effect of streamwise-periodic wall transpiration on turbulent friction drag. *J. Fluid Mech.* **576**, 425–444.

QUÉRÉ, D. 2008 Wetting and roughness. *Annu. Rev. Mater. Res.* **38**, 71–99.

REYSSAT, M., YEOMANS, J. M. & QUÉRÉ, D. 2008 Impalement of fakir drops. *Europhys. Lett.* **81**, 26006.

ROTHSTEIN, J. P. 2010 Slip on superhydrophobic surfaces. *Annu. Rev. Fluid Mech.* **42**, 89–109.

SAGONG, W., KIM, C., CHOI, S., JEON, W. P. & CHOI, H. 2008 Does the sailfish skin reduce the skin friction like the shark skin? *Phys. Fluids* **20**, 101510.

SAHLIN, A., ALFREDSSON, P. H. & JOHANSSON, A. V. 1986 Direct drag measurements for a flat plate with passive boundary layer manipulators. *Phys. Fluids* **29** (3), 696–700.

SAHLIN, A., JOHANSSON, A. V. & ALFREDSSON, P. H. 1988 The possibility of drag reduction by outer layer manipulators in turbulent boundary layers. *Phys. Fluids* **31** (10), 2814–2820.

SAMAHA, M. A., TAFRESHI, H. V. & GAD-EL HAK, M. 2011 Modeling drag reduction and meniscus stability of superhydrophobic surfaces comprised of random roughness. *Phys. Fluids* **23** (1), 012001.

SAVILL, A. M. & MUMFORD, J. C. 1988 Manipulation of turbulent boundary layers by outer-layer devices: skin-friction and flow-visualization results. *J. Fluid Mech.* **191**, 389–418.

SCHOPPA, W. & HUSSAIN, F. 1998 A large-scale control strategy for drag reduction in turbulent boundary layers. *Phys. Fluids* **10**, 1049.

SHUR, M., SPALART, P. R., STRELETS, M. & TRAVIN, A. 1999 Detached-eddy simulation of an airfoil at high angle of attack. In *Fourth International Symposium on Engineering Turbulence Modelling and Experiments*, pp. 669–678. Elsevier.

SIROVICH, L. & KARLSSON, S. 1997 Turbulent drag reduction by passive mechanisms. *Nature* **388**, 753–755.

SPALART, P. R. & ALLMARAS, S. R. 1992 A one-equation turbulence model for aerodynamic flows. *AIAA Paper 1992-04-39* **1** (2), 5–21.

SPALART, P. R., JOU, W. H. & ALLMARAS, M. S. S. R. 1997 Comments on the feasibility of les for wings and on hybrid RANS/LES approach. In *Proceedings of the First AFOSR International Conference on DNS/LES*, p. 137. Greyden Press.

SUDO, S., TSUYUKI, K., ITO, Y. & IKOHAGI, T. 2002 A study on the surface shape of fish scales. *JSME Intl J.* C **45** (4), 1100–1105.

TAY, C. M. J., KHOO, B. C. & CHEW, Y. T. 2015 Mechanics of drag reduction by shallow dimples in channel flow. *Phys. Fluids* **27** (3), 035109.

TRUESDELL, R., MAMMOLI, A., VOROBIEFF, P., VAN SWOL, F. & BRINKER, C. J. 2006 Drag reduction on a patterned superhydrophobic surface. *Phys. Rev. Lett.* **97** (4), 044504.

TU, S., ALIABADI, S., PATEL, R. & WATTS, M. 2009 An implementation of the Spalart–Allmaras DES model in an implicit unstructured hybrid finite volume/element solver for incompressible turbulent flow. *Intl J. Numer. Meth. Fluids* **59** (9), 1051–1062.

VELDHUIS, L. L. M. & VERVOORT, E. 2009 Drag effect of a dented surface in a turbulent flow. *AIAA Paper* 2009-3950; *San Antonio, Texas.*

WALSH, M. J. 1980 Drag characteristics of V-groove and transverse curvature riblets. In *Viscous Flow Drag Reduction*, pp. 168–184. AIAA.

WALSH, M. J. 1983 Riblets as a viscous drag reduction technique. *AIAA J.* **21**, 485–486.

WALSH, M. J. & LINDEMAN, A. M. 1984 Optimization and application of riblets for turbulent drag reduction. *AIAA Paper* 84-0347.

WALSH, M. J. & WEINSTEIN, L. M. 1978 Drag and heat transfer on surfaces with small longitudinal fins. *AIAA Paper* 78-1161.

WANG, Z., YEO, K. S. & KHOO, B. C. 2006 DNS of low Reynolds number turbulent flows in dimpled channels. *J. Turbul.* **7**, 37.

WESSELING, P. & OOSTERLEE, C. W. 2001 Geometric multigrid with applications to computational fluid dynamics. *J. Comput. Appl. Maths* **128** (1–2), 311–334.

ZHANG, X., SHI, F., NIU, J., JIANG, Y. G. & WANG, Z. Q. 2008 Superhydrophobic surfaces: from structural control to functional application. *J. Mater. Chem.* **18** (6), 621–633.

ZHOU, M., LI, J., WU, C. X., ZHOU, X. K. & CAI, L. 2011 Fluid drag reduction on superhydrophobic surfaces coated with carbon nanotube forests (cnts). *Soft Matt.* **7** (9), 4391–4396.